JOURNAL OF GEOPHYSICAL RESEARCH: SOLID EARTH, VOL. 118, 1–21, doi:10.1029/2012JB009442, 2013

High-resolution interseismic velocity data along the San Andreas Fault from GPS and InSAR

X. Tong,[1] D. T. Sandwell,[1] and B. Smith-Konter[2]

Received 11 May 2012; revised 6 September 2012; accepted 14 November 2012.

[1] We compared four interseismic velocity models of the San Andreas Fault based on GPS observations. The standard deviations of the predicted secular velocity from the four models are larger north of the San Francisco Bay area, near the creeping segment in Central California, and along the San Jacinto Fault and the East California Shear Zone in Southern California. A coherence spectrum analysis of the secular velocity fields indicates relatively high correlation among the four models at longer wavelengths (>15–40 km), with lower correlation at shorter wavelengths. To improve the short-wavelength accuracy of the interseismic velocity model, we integrated interferometric synthetic aperture radar (InSAR) observations, initially from Advanced Land Observing Satellite (ALOS) ascending data (spanning from the middle of 2006 to the end of 2010, totaling more than 1100 interferograms), with GPS observations using a Sum/Remove/Filter/Restore approach. The final InSAR line of sight data match the point GPS observations with a mean absolute deviation of 1.5 mm/yr. We systematically evaluated the fault creep rates along major faults of the San Andreas Fault and compared them with creepmeters and alignment array data compiled in Uniform California Earthquake Rupture Forecast, Version 2 (UCERF2). Moreover, this InSAR line of sight dataset can constrain rapid velocity gradients near the faults, which are critical for understanding the along-strike variations in stress accumulation rate and associated earthquake hazard.

Citation: Tong, X., D. T. Sandwell, and B. Smith-Konter (2013), High-resolution interseismic velocity data along the San Andreas Fault from GPS and InSAR, *J. Geophys. Res. Solid Earth*, *118*, doi:10.1029/2012JB009442.

1. Introduction

[2] The San Andreas Fault (SAF) System is a northwest trending transform plate boundary between the North America and Pacific plates. Major geological fault traces along the SAF are shown in Figure 1 in an oblique Mercator projection. The plate velocity between the North America and Pacific plates is about 45 mm/yr, determined from global plate motion models [*Demets et al*., 1990, 1994]. In Central California, the geological and geodetic slip rates of the SAF consistently suggest that 70–80% of the plate motion is accommodated by the SAF [*Noriega et al*., 2006; *Rolandone et al*., 2008]. In Southern California, the SAF splays into three main branches, the Elsinore Fault, the San Jacinto Fault, and the San Andreas Fault, which distribute about 45 mm/yr of strike-slip motion over a 200 km region. To the north of the creeping section, the SAF diverges offshore slipping at 25 mm/yr, while the paralleling Hayward and Calaveras faults absorb about 8 mm/yr of the dextral wrenching motion [*Lienkaemper and Borchardt*, 1996; *Segall*, 2002]. A recent summary of the geological and geodetic slip rates of the SAF can be found in *Molnar and Dayem* [2010].

[3] GPS measurements across the North American-Pacific Plate boundary are providing decade and longer time-series at 2 to 3 mm level precision from which surface velocity estimates are derived. One of the goals of these models is to provide strain rate estimation and to forecast seismicity rate. Several geodetic research groups have used these point velocity measurements to construct large-scale maps of crustal velocity. Since the typical spacing of GPS stations is about 5–10 km, an interpolation method or physical model must be used to compute a continuous vector velocity model that can be differentiated to construct a strain-rate map. Four approaches are typically used to develop strain maps: isotropic interpolation, interpolation guided by known faults, interpolation of a rheologically-layered lithosphere, and analytically determined strain rates derived from a geodetically constrained block model in an elastic half-space.

[4] The earliest interpolation studies used discrete GPS observations directly to obtain a spatially continuous horizontal velocity field and strain rate [*Frank*, 1966; *Shen et al*., 1996]. This method makes no assumptions on the location of a fault and does not need to solve for fault slip rates and locking depths when characterizing the strain field. Unknown faults (e.g., blind thrust faults), if accommodating enough strain, might be manifested through this method.

[1]Institution of Geophysics and Planetary Physics, Scripps Institution of Oceanography, University of California, San Diego, California, USA.
[2]Department of Geological Sciences, University of Texas at El Paso, El Paso, Texas, USA.

Corresponding author: X. Tong, Institution of Geophysics and Planetary Physics, Scripps Institution of Oceanography, University of California, San Diego, 8800 Biological Grade, San Diego, CA 92037-0225, USA. (xitong@ucsd.edu)

©2012. American Geophysical Union. All Rights Reserved.
2169-9313/13/2012JB009442

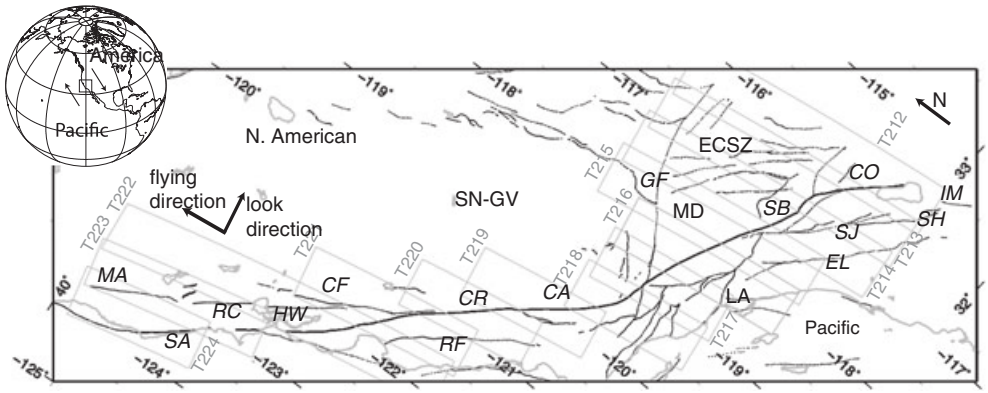

Figure 1. A map of the San Andreas Fault in California in oblique Mercator projection. The gray boxes with track numbers outline the area covered by 13 ALOS ascending tracks. The radar flying direction and look direction are marked. The black lines show the geological fault traces. Two-character labels with italicized font correspond to major faults mentioned in this paper: MA-Maacama fault, SA-San Andreas Fault, RC-Rodgers Creeks fault, HW-Hayward fault, CF-Calaveras fault, RF-Riconada fault, CR-creeping section, CA-Carrizo segment, GF-Garlock Fault, SB-San Bernardino segment, CO-Coachella segment, SJ-San Jacinto Fault, EL-Elsinore Fault, SH-Superstition Hills Fault, IM-Imperial Fault. Names with regular font are geographic locations: SN-GV-Sierra Nevada Great Valley, LA-Los Angeles basin, MD-Mojave desert, ECSZ-East California shear zone.

Freed et al. [2007] explored the relationship between occurrence of the $M > 6$ earthquakes and the stress changes induced by coseismic, postseismic, and interseismic deformation. Their interseismic stress accumulation rates were calculated directly from SCEC Crustal Motion Map (CMM3). *Kreemer et al*. [2003] constructed a global model for horizontal velocity and horizontal strain rate over major plate boundaries. They derived the velocity field from a least-squares interpolation method using bicubic Bessel splines. *Hackl et al*. [2009] developed a new interpolation procedure to compute strain directly from dense GPS networks and applied it to the interseismic deformation in Southern California and coseismic deformation of earthquakes. While these approaches have produced maps of the first-order strain rate field, the main issue is that in places where fault location information is not used, the spacing of GPS data is insufficient to accurately map the high strain concentrations along major faults.

[5] The second main strain rate modeling approach uses GPS observations to constrain fault slip rate and locking depths through model parameterization assuming a known set of fault locations. In these studies, model parameters are usually derived from minimization of the residual between the GPS observations and model prediction. An incomplete list of these models follows: *McCaffrey* [2005] represented the active deformation of the southwestern United States with rotating, elastic-plastic spherical caps. *Meade and Hager* [2005a, 2005b] estimated the moment accumulation rate from an elastic block model of interseismic deformation on the SAF constrained by GPS measurements. *Smith-Konter and Sandwell* [2009] used a semi-analytic viscoelastic earthquake cycle model to simulate the moment accumulation rate and stress evolution of the SAF over a thousand years [*Smith and Sandwell*, 2003, 2004, 2006]. *Shen and Jackson* [2005] modeled the surface deformation of Southern California using an elastic block model, which did not strictly enforce the continuity of fault slip rate on adjacent fault segments. *Parsons* [2006] constructed a finite element model of California by considering surface GPS velocity, crustal thickness, geothermal gradient, topography, and creeping faults. *Bird* [2009] incorporated community geologic, geodetic, and stress direction data to constrain the long-term fault slip rates and distributed deformation rates with a finite element model. It is worth noting that a deep dislocation underneath active faults is not a unique representation of the strain accumulation pattern everywhere in California. It has been proposed that the geodetic data may be explained to first order by simple shear across a 135 km wide shear zone [*Savage et al*., 1998; *Pollitz and Nyst*, 2005] in the San Francisco Bay region.

[6] A recent analysis of 17 strain rate models for the SAF has shown that GPS data alone cannot uniquely resolve the rapid velocity gradients near faults [*Hearn et al*., 2010]. The standard deviation of the strain models reveals a large discrepancy close to the fault, which can be caused by the different interpolation schemes used in constructing the strain models from discrete GPS measurements. *Baxter et al*. [2011] investigated the techniques to derive strain from discrete GPS velocity vectors and its inherent limitations. Incorporating Interferometric Synthetic Aperture Radar (InSAR) data along with GPS data has proven to be important to constrain high resolution kinematics over tectonically active regions [*Fialko*, 2006; *Burgmann et al*., 2007; *Ryder and Burgmann*, 2008].

[7] In this paper, we first evaluate the mean and standard deviation of four independent models to show that the GPS-derived interseismic velocity models are coherent at wavelengths greater than 15–40 km. Second, we develop a method to integrate InSAR data with GPS observations to recover the high-resolution interseismic velocity of the SAF. Third, we evaluate errors in the InSAR line of sight (LOS) data by comparing it to GPS measurements. (The InSAR

LOS data and their uncertainties are available at ftp://topex.ucsd.edu/pub/SAF_model/insar). Finally, we use this dataset to estimate the fault creep rates along the SAF and the other major faults systematically and compare this estimation with 115 ground-truth observations such as creepmeters and alignment arrays.

2. Evaluation of Interseismic Velocity Models Based on GPS Measurements

[8] To establish the accuracy and resolution of available interseismic velocity models, we compared four independent models based primarily on GPS observations. These models are products from a comprehensive strain rate comparison analysis [*Hearn et al*., 2010] and all the models are accessible through the following ftp site ftp://topex.ucsd.edu/pub/sandwell/strain/. The four models are:

1. H-model: *Meade and Hager* [2005a] developed a block model of Southern California constrained by the SCEC CMM3 GPS velocity. This was refined by *Loveless and Meade* [2011]. Their block models considered the block rotation and both the fault-parallel and fault-normal steady-state slip on block-bounding faults. They estimated the effective locking depths on some of the fault segments, and used results from previous studies on other fault segments.
2. M-model: *McCaffrey* [2005] represented active deformation of the southwestern United States with rotating, elastic-plastic spherical caps. The GPS velocity field was modeled as a result of rigid block rotations, elastic strain on block-bounding faults, and slip on faults within blocks (i.e., permanent strain).
3. Z-model: *Zeng and Shen* [2010] inverted regional GPS observations to constrain slip rates on major faults in California based on Okada solutions. Their model simulates both block-like deformation and elastic strain accumulation.
4. S-model: *Smith-Konter and Sandwell* [2009] developed a three-dimensional semi-analytic viscoelastic model to simulate the full earthquake cycle including interseismic deformation, coseismic displacement from past earthquakes, and postseismic relaxation following earthquakes. The slip rate was adopted from geologic studies and the apparent locking depth was estimated from the regional GPS velocity field. The model is fully three-dimensional and the vertical component of the GPS vectors is also used in the adjustment. In this study, we improve the original model by adding a grid of residual velocity using a spline fitting method [*Hackl et al*., 2009].

[9] We use two approaches to establish the similarities and differences among these four models. First we compute the mean and standard deviations of the horizontal components of the models and then we evaluate the spectral coherence among the models.

2.1. Standard Deviations

[10] Figure 2 shows the mean velocity and standard deviations of the four different GPS models. All the models are gridded at 0.01° pixel spacing with the *GMT surface* command. We adjusted each velocity model by subtracting its mean so that they reflect the same reference. The mean value of these models (2.5 mm/yr contour interval) shows a right lateral shear along SAF and the East California shear zone and transpression motion over the Mojave segment of SAF. At the creeping section, the velocity changes sharply, indicating a low degree of coupling of the fault, while in Southern and Northern California, the right lateral shear motion is taken up by multiple parallel faults. The standard deviation (0.5 mm/yr contour interval) ranges from 0 to 2 mm/yr for both the east and north velocity, except at the creeping section where it exceeds 3 mm/yr. The smaller standard deviation ($<$1.0 mm/yr) indicates good agreement among models and larger standard deviation ($>$1.0 mm/yr) emphasizes the areas of largest discrepancy, such as the creeping section, north of the San Francisco Bay area, the San Jacinto Fault and the East California Shear Zone in Southern California. A similar kind of effort to compare independent model results has been carried out in a previous California strain rate comparison [*Hearn et al*., 2010].

[11] There are several factors that could explain the discrepancies among the GPS models. First, the discrepancies could be caused by the imprecise location of a fault or inaccurate fault dip, which could be resolved by using a more accurate fault model. On the creeping part of SAF (e.g., Hayward fault, Calaveras fault, creeping sections over Central California), the fault trace could be more accurately constrained by velocity steps revealed by InSAR observations. Second, the discrepancy could be caused by different locking depth and slip rate used in different models. As shown in Figure 2, there is a larger uncertainty among the models north of the San Francisco Bay area. For example, *McCaffrey* [2005] inferred that the Maacama Fault has a slip rate of 7.4 mm/yr and has a significant fraction of fault creep. *Smith-Konter and Sandwell* [2009] inverted a 10 mm/yr slip rate and 8.6 km locking depth along the Maacama Fault. Likewise, 30 km east of the Maacama Fault resides the Green Valley Fault. *McCaffrey* [2005] inferred a 7.3 mm/yr slip rate with a large fraction of fault creep along the Green Valley fault [*McCaffrey*, 2005, Figure 3a]. *Smith-Konter and Sandwell* [2009] estimated a slip rate of 6.4 mm/yr with a locking depth 5 km along the same fault. This analysis illustrates that the current GPS velocity field is not able to distinguish a shallow locked fault from a creeping fault. For instance, we calculated two fault-parallel velocity profiles by changing the locking depth from 1 km to 5 km, for a constant slip rate of 7 mm/yr. The difference of the velocity profiles reaches a maximum of 1.6 mm/yr at 2 km from the fault trace and decreases to 0.2 mm/yr at 40 km from the fault. Thus, high resolution and high precision observations close to the fault are needed to constrain the slip rates and locking depths of parallel faults. Third, in the area where significant surface creep occurs, like the creeping section in Central California, the locking depth is difficult to constrain from GPS alone.

2.2. Cross-Spectrum Analysis

[12] The second method used to establish the similarities and differences among these four models was to perform a cross-spectral analysis among pairs of models (Figure 3). Based on the above analysis, we expect the model pairs to show good agreement at longer wavelengths and poor agreement at shorter wavelengths. The coherence is a measure of the degree of relationship, as a function of frequency,

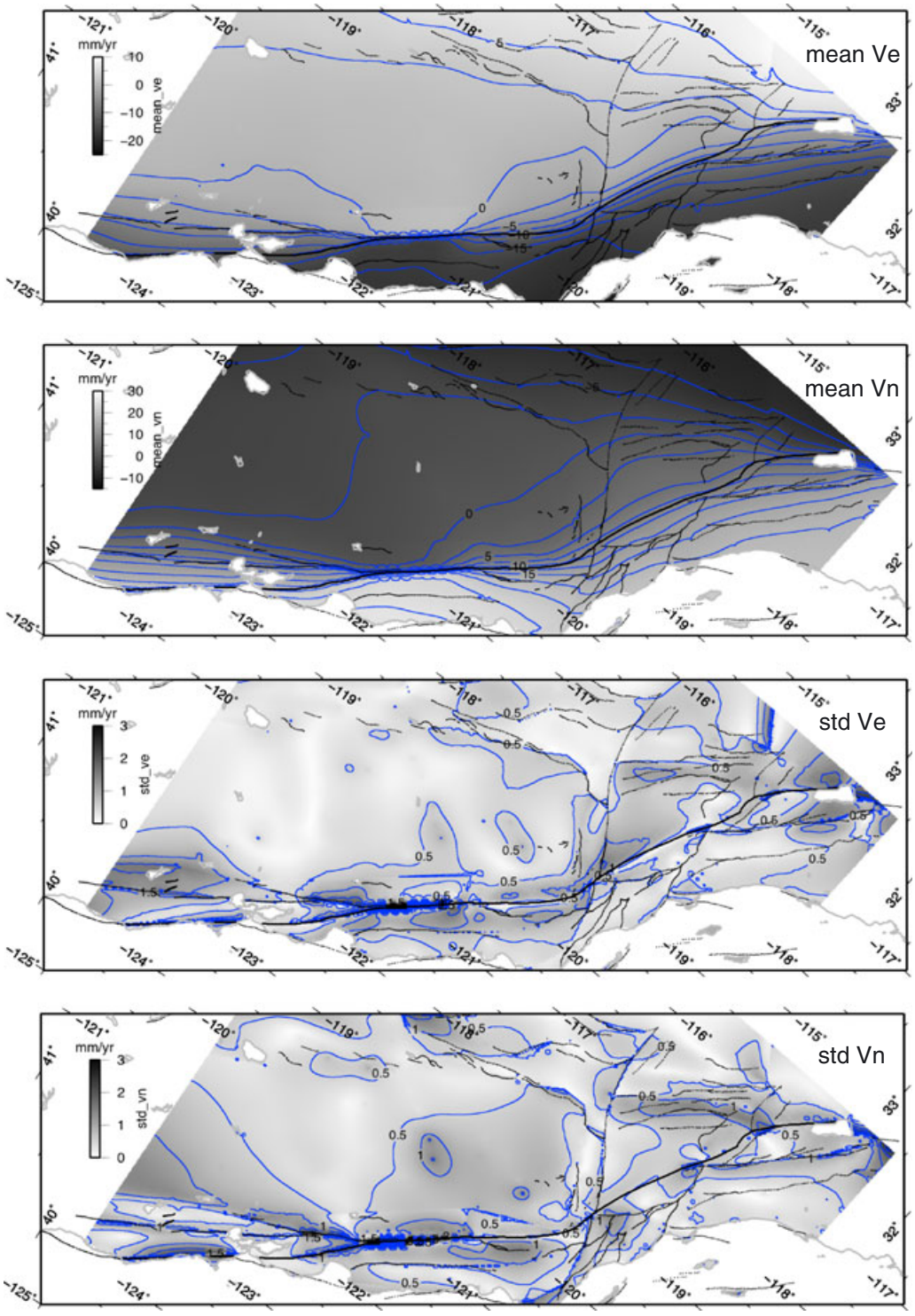

Figure 2. Cross comparison of the four independent GPS velocity models of the SAF in geographic coordinates. The plots are in oblique Mercator projection with contour lines in blue. (a) Mean of the east component of the velocity models. (b) Mean of the north component of the velocity models. (c) Standard deviation of the east component of the velocity models. (d) Standard deviation of the north component of the velocity models. The contours are at 2.5 mm/yr interval for Figures 2a and 2b and at 0.5 mm/yr interval for Figures 2c and 2d. The black lines show the geological fault traces.

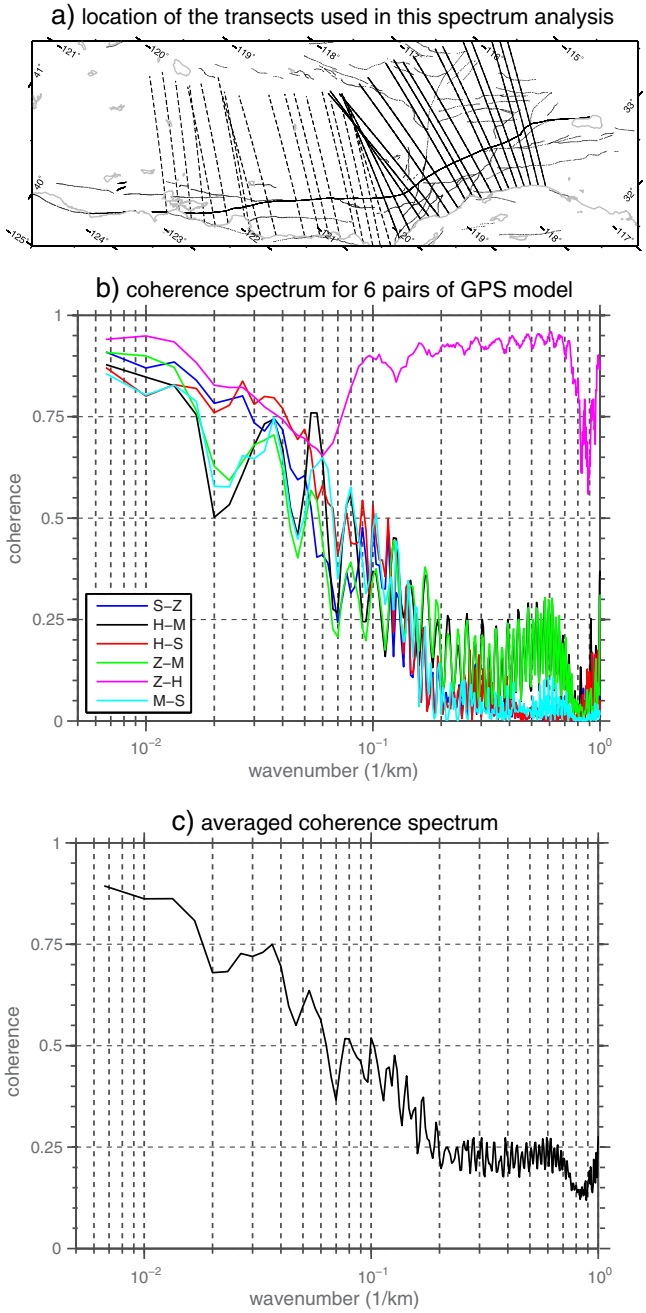

Figure 3. (a) The 37 transect lines (solid lines and dashed lines) show the profiles used in the coherence spectrum analysis. The 18 solid transect lines show the profiles used in the power spectrum analysis (Figure 15). (b) Coherence as a function of wave number for four independent GPS-derived models. The coherence spectrum for six pairs of the GPS velocity models are compared here: H-model from *Meade and Hager* [2005a]; M-model from *McCaffrey* [2005]; Z-model from *Zeng and Shen* [2010]; S-model from *Smith-Konter and Sandwell* [2009]. (c) Average of the six pairs of coherence spectra from GPS velocity models.

between two time series. This crossover wavelength is needed to determine the filter wavelength in the GPS/InSAR integration step (section 3.2). We used Welch's modified periodogram approach [*Welch*, 1967] as implemented in MATLAB to estimate the coherence for 37 LOS profiles crossing the plate boundary. There are three steps in this approach:

1. Project horizontal velocity components into LOS velocity for each of the four GPS models. In this cross-spectrum analysis the look direction of radar is taken to be constant (81° azimuth, 37° from vertical). In the InSAR/GPS integration (section 3), we take into account that the look direction of radar varies across satellite track.
2. Extract across-fault profiles spaced at 10–20 km intervals in the north-south direction. Each profile starts at the coastline and extends 300 km inland. The profiles that have gaps (no data) are discarded. We extract 37 profiles from each model (transect lines in Figure 3a) using linear interpolation with a pixel spacing of 0.2 km.
3. Concatenate the 37 profiles end-to-end to form one vector for each model. Compute the magnitude-squared coherence using Welch's averaged periodogram method. In order to avoid artifacts associated with jumps where the 37 profiles abut each other, we first applied a 300 km long Hanning-tapered window to each profile. Then the periodogram for the 37 profiles was computed and averaged to get the final estimate of the coherence spectrum.

[13] Figure 3b shows the coherence as a function of wave number for all the possible combinations within the four GPS models. Because the profiles only sample 300 km in across-fault distance, the coherence estimated over wavelengths greater than 150 km is not reliable. Below 150 km wavelengths however, the coherence estimates show several interesting features: To first order, the coherence among GPS models is high (>0.8) between wavelengths of 150 and 66 km and then drops to 0.5 at about 20 km wavelengths. This wavelength is expected because it corresponds to the characteristic spacing of the GPS receivers. There is a high coherence of 0.8 at the 33–50 km wavelength among Z, H, and S models. In contrast, the coherence between M-model and other models has a relatively low value of 0.55 at the same scale. While all the other models show lower correlation at smaller length scales, the correlation between Z-model and H-model reaches 0.9 between wavelengths of 1 and 10 km. We suspect that this high coherence reflects the fact that these two models use nearly identical fault geometry and have short wavelength signals that are common at creeping faults. We found that the averaged coherence spectrum falls off to 0.7 approximately at 40 km and to 0.5 at 20 km (Figure 3c).

3. Integration of InSAR and GPS

[14] The approach for combining multiple interferograms of a region with GPS observations has four primary steps and is based on a study by *Wei et al*. [2010]. The first step is to sum up the available interferograms, keeping track of the total time span of the sum to compute a LOS velocity. This stacking will enhance the signal-to-noise ratio because, for example, the residual tropospheric noise is uncorrelated for a time span longer than 1 d [*Williams et al*., 1998; *Emardson et al*., 2003]. The second step is to project a fine-sampled interseismic velocity field based on the GPS measurements

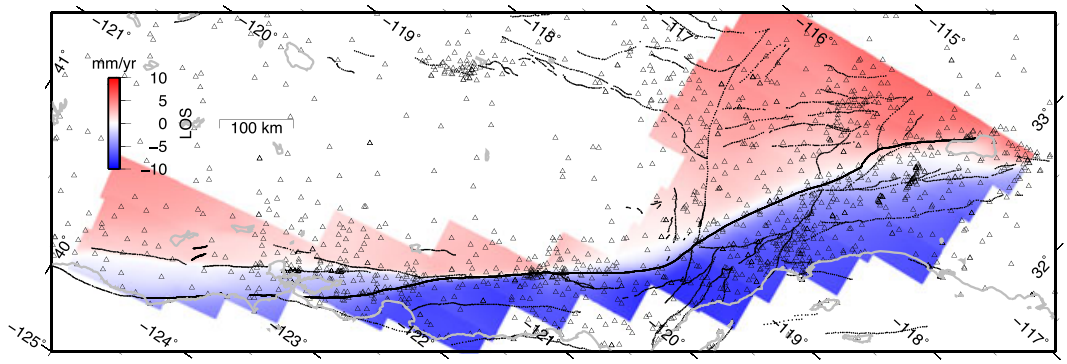

Figure 4. Crustal velocity model in LOS velocity based on regional GPS velocity field [*Smith-Konter and Sandwell*, 2009] in oblique Mercator projection. The colors represent the LOS velocity field along 13 ALOS ascending tracks represented by radar swaths (Figure 1). The radar flying direction and look direction are marked in Figure 1. Positive velocities (reds) show the ground moving relatively away from the satellite. The small triangles are the GPS stations used to constrain the velocity model. The black lines show the geological fault traces.

into the LOS velocity of the interferogram (Figure 4) and to remove this model from the stack. A block model or viscoelastic model is necessary to integrate the sparse GPS velocities with dense InSAR LOS data in the spatial domain. For this study, we use a modified version of the S-model to provide a long-wavelength basis for integration of GPS and InSAR. The horizontal components of this velocity model are used in the projection since the vertical component are not well constrained by the current vertical velocity of GPS. The third step is to high-pass filter the residual stack to further suppress errors at length scales much greater than the crossover wavelength. This crossover wavelength was selected based on the coherence analysis above. The final step is to add the GPS-based model back to the filtered stack to recover the full LOS velocity. The acronym for this integration approach is called "SURF" (Sum/Remove/Filter/Restore). As shown in Figure 5, it is clear that the recovered InSAR LOS velocity map provides shorter wavelength information not captured by the GPS-based model (compare to Figure 4). The details of the result shown in Figure 5 are discussed in section 4.

3.1. InSAR Data Processing

[15] We processed 13 ascending tracks of Advanced Land Observing Satellite, Phased Array type L-band Synthetic Aperture Radar (ALOS PALSAR) interferograms spanning from the middle of 2006 to the end of 2010 in preparation for stacking. More than 1100 interferograms were processed to cover the entire SAF. We performed the InSAR data processing and the GPS/InSAR integration using GMTSAR software, which is publicly available from http://topex.ucsd.edu/gmtsar [*Sandwell et al*., 2011]. We processed the SAR data on a frame-by-frame basis so that the frame boundaries of the interferograms match seamlessly along track (Figure 5). By doing so, we avoided discarding entire tracks of data and still processed other frames along the same track if the pulse repetition frequency changes along track or the SAR data in one of the frames were missing or problematic. A summary of the SAR dataset used in the analysis is in Table 1. The baseline-time plots of the SAR data used in this study can be accessed through the following site: ftp://topex.ucsd.edu/pub/SAF_models/insar/basetime.

[16] The main processing steps are (1) preprocessing, (2) SAR image formation and alignment, (3) interferogram formation and topographic phase correction, (4) phase unwrapping, and (5) GPS/InSAR integration. We discuss details of steps (2) to (5) in the following paragraphs. All of these steps are done in the radar coordinates for consistency. After GPS/InSAR integration, we projected the products into geographic coordinates with pixel spacing of 3 arc seconds (∼90 m) for further analysis.

[17] As shown in an example baseline-time plot (Figure 6), the perpendicular baseline of the Advanced Land Observing Satellite (ALOS) satellite drifted from –1000 m to 1000 m (June 2007 to April 2008) and then was reset to –7000 m in the middle of 2008, when it then started to drift again. Subsequently, short baseline and long time-span interferograms were not available until the middle of 2010. Unfortunately, the satellite stopped working due to power issues in April 2011, so for most frames, fewer than 20 interferograms are available for stacking. The drifting orbit also makes it difficult to align all the images using conventional methods.

[18] As shown in Figure 6, the baseline between the two SAR images can reach several thousand meters, thus a direct alignment of the images relying on the satellite trajectory is difficult. We adopted a "leap frog" approach [*Sandwell and Sichoix*, 2000; *Sandwell et al*., 2011] to align every image in this baseline-time plot to one image (called "super master"). Taking Figure 6 as an example, we first chose an image as "super master" (10024 in this case). We then aligned the images that were close to (i.e., perpendicular baseline $<$1000 m) the "super master" in the baseline-time domain to the "super master" (marked as Primary match in Figure 6). After alignments, the images were registered in the same coordinates as the "super master" within one pixel accuracy, thus they can be treated as new master images (called "surrogate master"). Then we aligned other images (marked as Secondary match in Figure 6) that are far from the "super master" in the baseline-time domain to the "surrogate master".

[19] Because the interseismic motion is subtle compared to the atmospheric noise, we chose interferometry pairs with

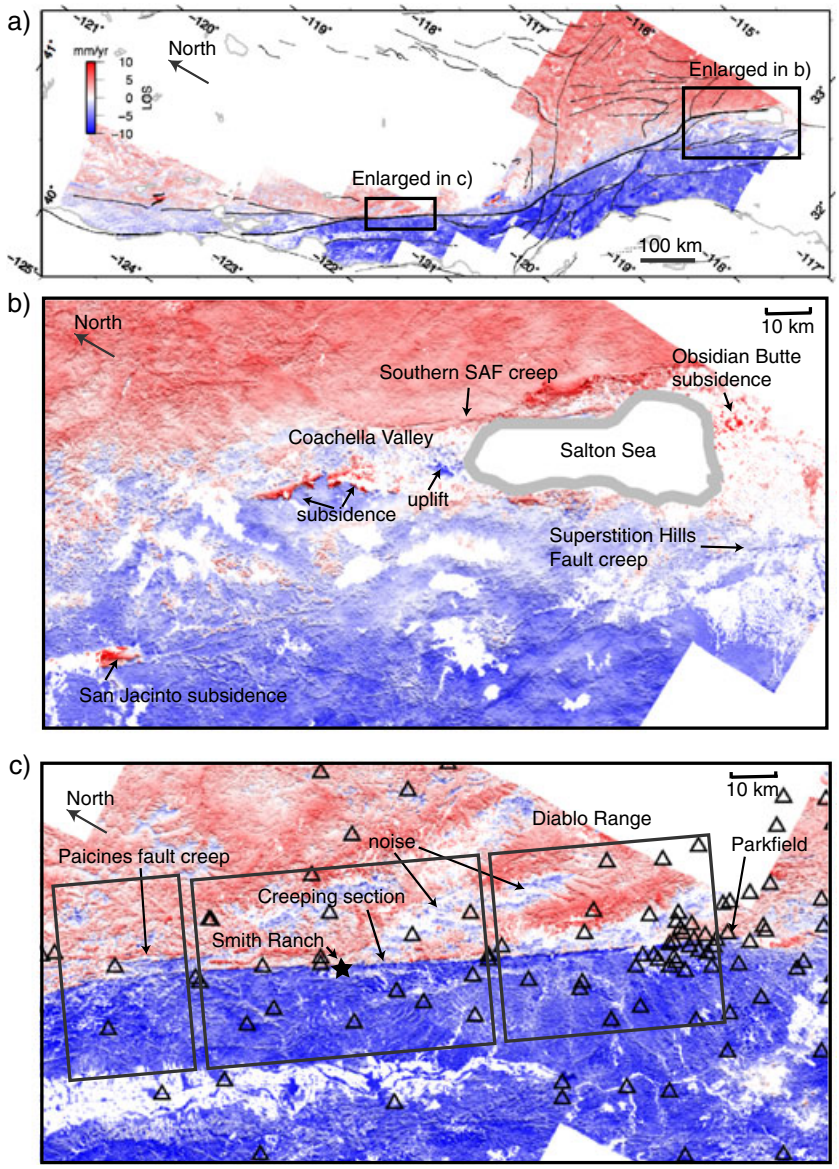

Figure 5. (a) Interseismic deformation of the SAF derived from integrating the GPS observations with ALOS radar interferograms (2006.5–2010). The radar flying direction and look direction are marked in Figure 1. Positive velocities (reds) show the ground moving away from the satellite. The shading highlights the gradient in the velocity field. The areas with low coherence and large standard deviation (>6 mm/yr) are masked. GPS sites are shown as triangles. (b) Southern part of the SAFS shows the broad transition in velocity across San Andreas and San Jacinto. (c) Central section of the SAFS shows the sharp velocity gradient across the creeping section. The black star marks the location of the Smith Ranch. The black boxes mark the locations of the velocity profiles shown in Figure 12. A full resolution version of this LOS velocity map and its relationship to faults and cultural features can be downloaded as a KML-file for Google Earth from the following site: ftp://topex.ucsd.edu/pub/SAF_models/insar/ALOS_ASC_masked.kmz.

long time intervals (>1 yr) and with small perpendicular baselines (<600 m) to enhance the signal-to-noise ratio (Figure 7). The summations of the perpendicular baselines are minimized to reduce the topographic error (Table 1). Topographic phase is removed using digital elevation model obtained from Shuttle Radar Topography Mission (SRTM1) [*Farr et al*., 2007]. The relative height error of SRTM1 over North America is estimated to be 7 m. In addition, the height measured by SRTM1 is an effective height. In the presence of vegetation or snow or very dry soil, C-band radar waves on board SRTM reflected at a different effective height than the L-band radar on board ALOS [*Farr et al*., 2007], which can cause an error in digital elevation model (DEM) on the order of 5–10 m. The relationship between LOS velocity error dv and the DEM error dh after stacking is: $dv = (4\pi/\lambda)\left(\sum B^i_{\mathrm{perp}}/\sum_{i=1}^{N}\Delta t^i\right) \times ((r_e + h)/\rho b \sin\theta) dh$ [*Sandwell et al*., 2011, Appendix C] , where r_e is radius of the Earth

Table 1. Data Information About ALOS Ascending Tracks

Track	Frame	Sum of Perpendicular Baseline (m)	Number of Interferograms	Total Time Span (days)
224	780	–16	28	22,724
224	770	–16	28	22,724
224	760	–82	26	20,930
223	750	148	16	14,674
223	760	148	16	14,674
223	770	148	16	14,674
223	780	148	16	14,674
222	780	–146	23	18,676
222	770	–146	23	18,676
222	760	–146	23	18,676
222	750	–146	23	18,676
222	740	–146	23	18,676
222	730	–146	23	18,676
222	720	9	19	17,250
222	710	9	19	17,250
221	710	–34	15	12,374
221	720	30	8	7314
221	730	–104	14	11,362
221	740	–104	14	11,362
220	700	32	14	13,110
220	710	32	14	13,110
220	720	32	14	13,110
219	690	13	29	24,932
219	700	13	29	24,932
218	670	3	23	19,090
218	680	3	23	19,090
218	690	3	23	19,090
217	670	15	13	11,914
217	680	15	13	11,914
217	690	15	13	11,914
216	660	7	24	20,838
216	670	7	24	20,838
216	680	–60	23	19,826
216	690	–60	23	19,826
215	650	–65	9	6900
215	660	–6	11	9200
215	670	–6	11	9200
215	680	–6	11	9200
215	690	–104	16	13,708
215	700	–104	16	13,708
214	650	1	21	18,952
214	660	1	21	18,952
214	670	1	21	18,952
214	680	1	21	18,952
214	690	1	21	18,952
214	700	1	21	18,952
213	650	–228	33	28,428
213	660	–228	33	28,428
213	670	–228	33	28,428
213	680	–228	33	28,428
213	690	–228	33	28,428
213	700	–228	33	28,428
212	650	–1	10	9384
212	660	–1	10	9384
212	670	–1	10	9384
212	680	–1	10	9384
212	690	–151	9	8418
212	700	–151	9	8418

(6371 km), ρ is the distance from the radar satellite to the ground (800 km), b is the distance from the radar satellite to the center of the Earth (7171 km), λ is the radar wavelength (0.236 m), h is the elevation of the ground (1 km), θ is the radar look angle (34°), i denotes the ith interferogram, N is the total number of interferograms, $\sum B^i_{\text{perp}} / \sum_{i=1}^{N} \Delta t^i$ is the summation of perpendicular baseline over the summation of the time span for all the interferograms(10 m/10,000 days). See Table 1 for exact values used in the data processing. Using the above representative values denoted in the parenthesis and taking DEM error dh to be 10 m, we estimated a bias in LOS velocity dv of 0.4 mm/yr. The interferograms were filtered with a Gaussian low-pass filter at 200 m full wavelength and subsequently subsampled at 2 pixels in range (15.6 m projected on the ground) by 4 pixels in azimuth (13.2 m). We then applied a Goldstein filter [*Goldstein and Werner*, 1998] to the interferograms to obtain the final interferogram in wrapped phase.

[20] In order to identify the small-scale deformation signal, we must first eliminate the errors associated with the automatic unwrapping. Sometimes automatic unwrapping provides inaccurate results (known as "phase jumps"), especially where there are cultivated fields, sand dunes, or water. We devised an iterative approach to overcome difficulties that occasionally occur in the automatic phase unwrapping of InSAR phase data (Figure 8). Initially, we unwrapped the phase of each interferogram using the SNAPHU software [*Chen and Zebker*, 2000] (SNAPHU stands for Statistical-Cost, Network-Flow Algorithm for Phase Unwrapping). Next, we constructed a trend from the unwrapped phase using *GMT functions grdtrend*, *grdfilter*, *surface*. Then we removed the trend from the original wrapped phase to derive the "fluctuation phase". If the fluctuation phase is within $\pm\pi$, we add fluctuation to the trend to get a complete unwrapped phase and the unwrapping is done; If not, we reestimate the trend and iterate. We unwrapped the phase by hand for some extremely difficult cases, like the interferograms over the Imperial Valley.

3.2. The SURF Approach

[21] After unwrapping the phase of each interferogram, we carried out the GPS/InSAR integration step using the SURF approach [*Wei et al.*, 2010] shown as Figure 9. We discuss

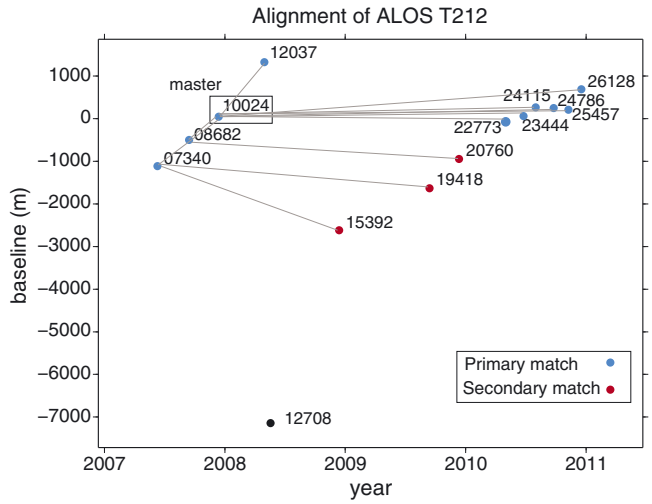

Figure 6. Example perpendicular baseline versus time plot showing the "leap-frog" alignment approach taken prior to forming the interferograms. The track number is 212 and the orbital indices are shown as a 5 digit number in the plot. Image 10024 is boxed, representing the super master image. Primary matches (those that plot close to the super master in the baseline-time domain) are represented by blue dots. Secondary matches are represented by red dots.

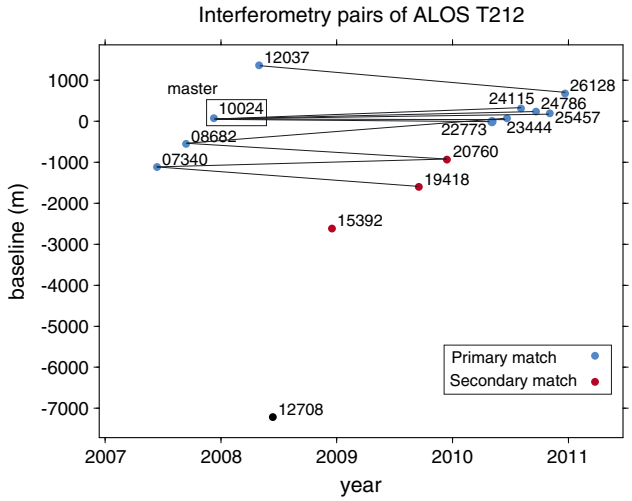

Figure 7. Example perpendicular baseline versus time plot showing interferometric pairs used in the stacking. The track number is 212 and the orbital indices are shown as 5 digit numbers in the plot.

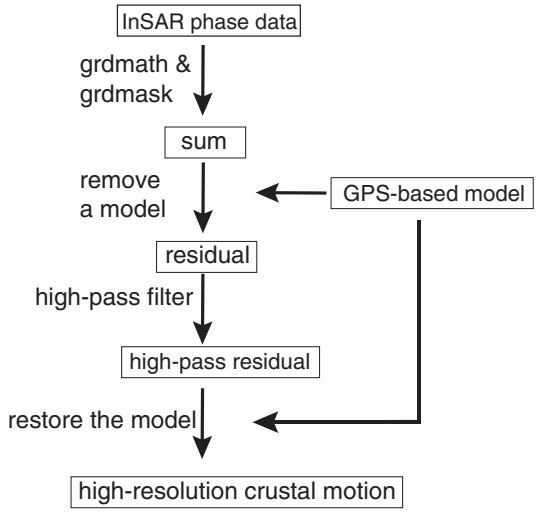

Figure 9. Flowchart of combining InSAR stacks with GPS observations [*Wei et al.*, 2010].

the advantages of this integration approach in section 3.3 Here we describe each step in detail:

1. Sum the unwrapped phase of each interferogram $\varphi^i(x,\Delta t^i)$, i denotes the ith interferogram, x is a two-dimensional spatial variable in radar coordinates. Scale the summation with respect to their corresponding time interval Δt^i using the formula $\bar{\varphi}(x) = \sum_{i=1}^{N} \varphi^i(x,\Delta t^i) / \sum_{i=1}^{N} \Delta t^i$, and scale it from phase in radius to velocity in millimeters per year. $\bar{\varphi}$ is the average LOS velocity. N is the total number of interferograms. Make a coherence mask (>0.06) from a stack of coherence maps. Make a land mask if applicable. Make a mask to isolate the anomalous deformation signals when necessary. By stacking we cancel out the random atmospheric noise and nonsteady ground movement to recover the steady state interseismic deformation.
2. Remove the GPS model $M(x)$ from the stacked phase to obtain the residual phase by $\bar{\varphi}(x) - M(x)$, where $M(x)$ is the interseismic velocity model from GPS. The interseismic velocity model *Smith-Konter and Sandwell* [2009] is projected from geographic coordinates (longitude-latitude) into radar coordinates (range-azimuth). The two-component (local east-north) velocity of each pixel is converted into LOS velocity considering variable radar looking directions across track (Figure 4).
3. Filter the residual phase with a Gaussian high-pass filter $F_{\text{high}}(x)$ at the crossover wavelength by $[\bar{\varphi}(x) - M(x)] * F_{\text{high}}(x)$. *Wei et al.* [2010] used a crossover wavelength of 40 km inferred from typical spacing of GPS sites. We determined the filter wavelength based on a coherence spectrum analysis and found that 40 km is a good choice for the crossover wavelength. The optimal crossover wavelength may vary from location to location and warrants further investigation. The high-pass filtered residual $[\bar{\varphi}(x) - M(x)] * F_{\text{high}}(x)$ shows the small-scale difference between the InSAR LOS velocity and the GPS model prediction (Figure 10).
4. Restore the original interseismic velocity model $M(x)$ by adding it back to the filtered residual phase. Thus, $V_{\text{InSAR}}(x)$ combines the short wavelength signal from InSAR stacking and the long wavelength signal from GPS. Convolution is a linear operator, thus we have: $V_{\text{InSAR}}(x) = [\bar{\varphi}(x) - M(x)] * F_{\text{high}}(x) + M(x) = \bar{\varphi}(x) * F_{\text{high}}(x) + M(x) * F_{\text{low}}(x)$. $F_{\text{low}}(x)$ is the corresponding low-pass filter. The error from the GPS-based model after low-pass filtering is reduced to a level of 1 mm/yr as discussed in section

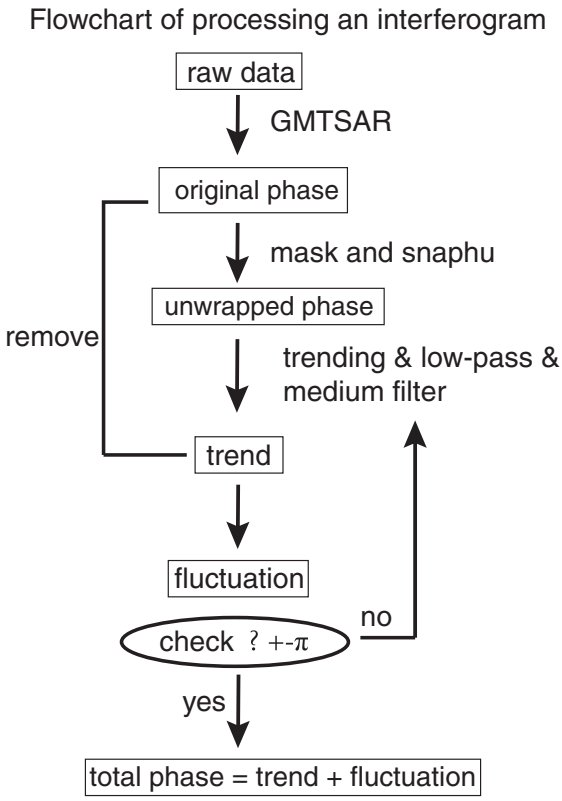

Figure 8. Flowchart for iterative phase unwrapping of a single interferogram.

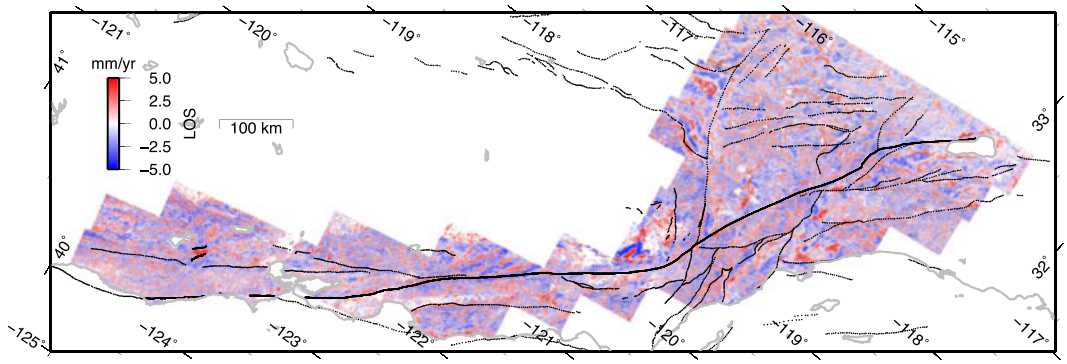

Figure 10. High-pass filtered residual velocity (2006.5–2010) along ALOS ascending tracks. This residual velocity reveals the discrepancy between the InSAR observations and GPS model prediction at short wavelength. For example, we found that the residual are significant along the creeping sections, the Garlock Fault, and the LA basin. A fine-tuned interseismic velocity model based on both InSAR and GPS observations should have smaller high-pass filtered residual velocity. Note that the residual could also be caused by nontectonic effects, such as ground water.

2, and the error from InSAR after high-pass filtering is evaluated in step 5.

5. We evaluated the errors in the InSAR data after high-pass filtering by calculating its standard deviations with the formula $\sigma_{InSAR}(x)=\sqrt{\left\{\sum_{i=1}^{N}\left[\left[(\varphi^i(x,\Delta t^i)/\Delta t^i)-V_{\mathrm{InSAR}}(x)\right]*F_{\mathrm{high}}(x)\right]^2\right\}/N}$ (Figure 11). Larger uncertainties could be due to unwrapping errors, atmospheric noise or deviations from steady state ground motion. The standard deviation varies spatially, ranging from <1 mm/yr to >10 mm/yr for some regions with an average value of ~ 3 mm/yr.

3.3. Advantage of this GPS/InSAR Integration Approach

[22] Although there are not many explicit studies on GPS/InSAR integration methods, almost every study using InSAR phase data to retrieve coseismic, postseismic, interseismic, and volcanic deformations relies on GPS to correct the long wavelength errors of InSAR phase data. We found that this integration method usually involves interpolation between GPS stations [*Gourmelen et al.*, 2010; *Johanson and Burgmann*, 2005; *Lyons and Sandwell*, 2003; *Peltzer et al.*, 2001; *Ryder and Burgmann*, 2008; *Wei et al.*, 2009]. For instance *Johanson and Burgmann* [2005] studied the interseismic slip rate on the San Juan Bautista segments of the SAF. For each interferogram, they removed a GPS-derived interseismic velocity model from interferogram phase data to obtain the so-called residual phase, then they fitted and removed a lower order polynomial from the residual phase, then they replaced the interseismic model back. The removal of an interseismic velocity model may facilitate phase unwrapping. We call this kind of integration approach the remove/correct/restore/stack method. *Wei et al.* [2009] used a very similar method but their procedure is remove/stack/correct/restore. The exact order of the processing steps does not matter much because of the linearity of these operations. In other studies the difference between the interferogram phase data and the co-located GPS measurements are used to construct a linear trend, which is subsequently removed from the InSAR phase data [*Fialko*, 2006; *Lundgren et al.*, 2009].

[23] In this study we used the SURF approach to integrate GPS and InSAR observations. This simple approach is an improvement based on the aforementioned method: the remove/correct/restore/stack method that has been used

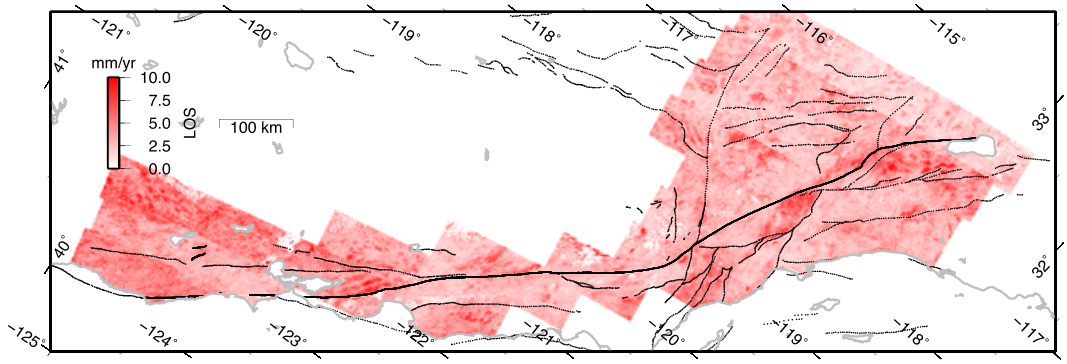

Figure 11. Standard deviation of the average LOS velocity (2006.5–2010) along ALOS ascending tracks. Larger uncertainties are found north of the San Francisco Bay area in Northern California, near the San Bernardino Mountain. The uncertainties could be due to unwrapping errors, atmospheric noise or deviations from steady-state ground motion. The standard deviation provides a measure of uncertainty of the high-resolution LOS velocity data and can be used in modeling the interseismic deformation.

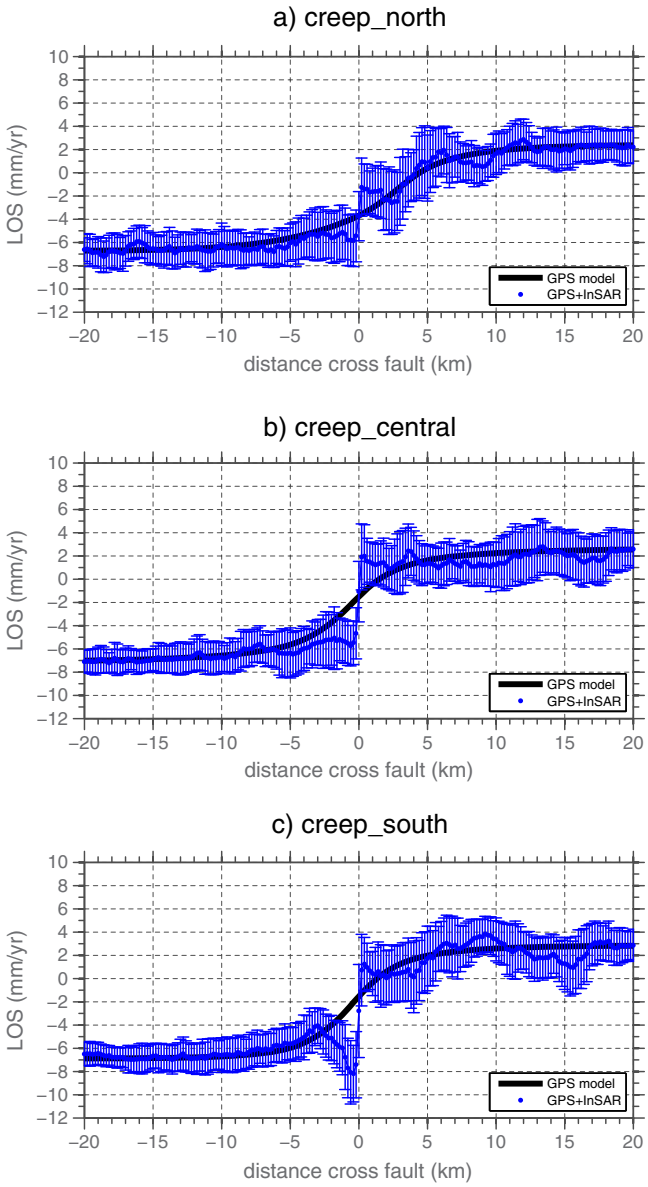

Figure 12. Averaged LOS velocity profiles perpendicular to the fault over Central California along the creeping section of the SAF (Figure 5c). The blue dots with 1 standard deviation error bars indicate the total LOS velocity, and the black lines are the GPS model. (a) Profile taken along the northern segment of the creeping section. (b) Profile taken along the central segment of the creeping section. (c) Profile taken along the southern segment of the creeping section.

extensively. Our approach has the following characteristics: (1) this method does not assume a particular form of the orbital error because the exact form of the first- or second-order polynomial is uncertain [*Gourmelen et al.*, 2010]. (2) The interpolation between GPS stations is realized by a physical model constrained by GPS velocity [*Smith-Konter and Sandwell*, 2009]. (3) The high-pass filter further improves the signal-to-noise ratio of the stacking by filtering out tropospheric and ionospheric noise. (4) The wavelength of the high-pass filter used in this study is determined by a cross-comparison of four independent interseismic velocity models (Figure 3). (5) The high-pass filtered residual data provide information on the inaccuracy of the current interseismic models. This method has the potential to be applied and developed in other InSAR studies.

4. Evaluation and Distribution of LOS Results

4.1. InSAR LOS Velocity Map

[24] Figure 5a shows the high-resolution interseismic velocity data ($V_{\mathrm{InSAR}}(x)$) along the SAF derived from integrating the GPS observations with ALOS radar interferograms (2006.5–2010). The areas with low coherence and large standard deviation (>6 mm/yr) are masked. Comparing this to GPS model (Figure 4), the recovered interseismic velocity data have greater variations including surface expression of the fault creep, localized deformation pattern related to nontectonic effect, and anomalous velocity gradient near active faults. These details of the velocity field are highlighted by shading the final grid weighted by its gradient. A full resolution version of this LOS velocity map and its relationship to faults and cultural features can be downloaded as a KML-file for Google Earth from the following site: ftp://topex.ucsd.edu/pub/SAF_models/insar/ALOS_387ASC_masked.kmz . A data file of longitude, latitude, LOS velocity, standard deviations of 388 of the LOS velocity, unit vector for LOS, can be obtained through ftp://topex.ucsd.edu/pub/SAF_model/insar. Next we discuss two subregions.

[25] Figure 5b shows the broad transition in velocity across the San Andreas and San Jacinto faults that is well studied [*Fialko*, 2006; *Lundgren et al.*, 2009]. Besides this large-scale feature, we note several interesting small-scale features. Shallow fault creep is apparent across the San Andreas Fault (∼4 mm/yr) near the Salton Sea [*Lyons and Sandwell*, 2003], as well as across the Superstition Hills fault (∼3 mm/yr) [*Wei et al.*, 2009]. There are several areas of rapid localized subsidence possibly due to groundwater extraction. For example, there is a large subsidence region around Indio, CA where subsidence has been documented by *Sneed and Brandt* [2007]. Other prominent examples of anomalous velocity occur along the Coachella valley west of SAF where prominent subsidence at >30 mm/yr, and uplift of ∼10 mm/yr just north of the Salton Sea, are observed (see Figure 5b). There is an interesting subsidence confined by a "step-over" structure along the San Jacinto Fault [*Wisely and Schmidt*, 2010]. The subsidence rate in this "step-over" reaches as high as ∼18 mm/yr, which is too large compared to the expected signal from tectonic extension. Localized subsidence is also apparent at Obsidian Butte (∼14 mm/yr) to the south of the Salton Sea [*Eneva and Adams*, 2010].

[26] Figure 5c shows the sharp velocity gradient across the creeping section, as well as the Calaveras fault along the central part of SAF [*Rosen et al.*, 1998; *Johanson and Burgmann*, 2005]. From this map, we identify that the southern end of the creeping section is at a "step-over" south to the Parkfield region (Figure 5c). We divided the creeping section into three segments: northern, central, and southern segments and took profiles across the fault. Three profiles are shown in Figure 12. InSAR observations resolved the

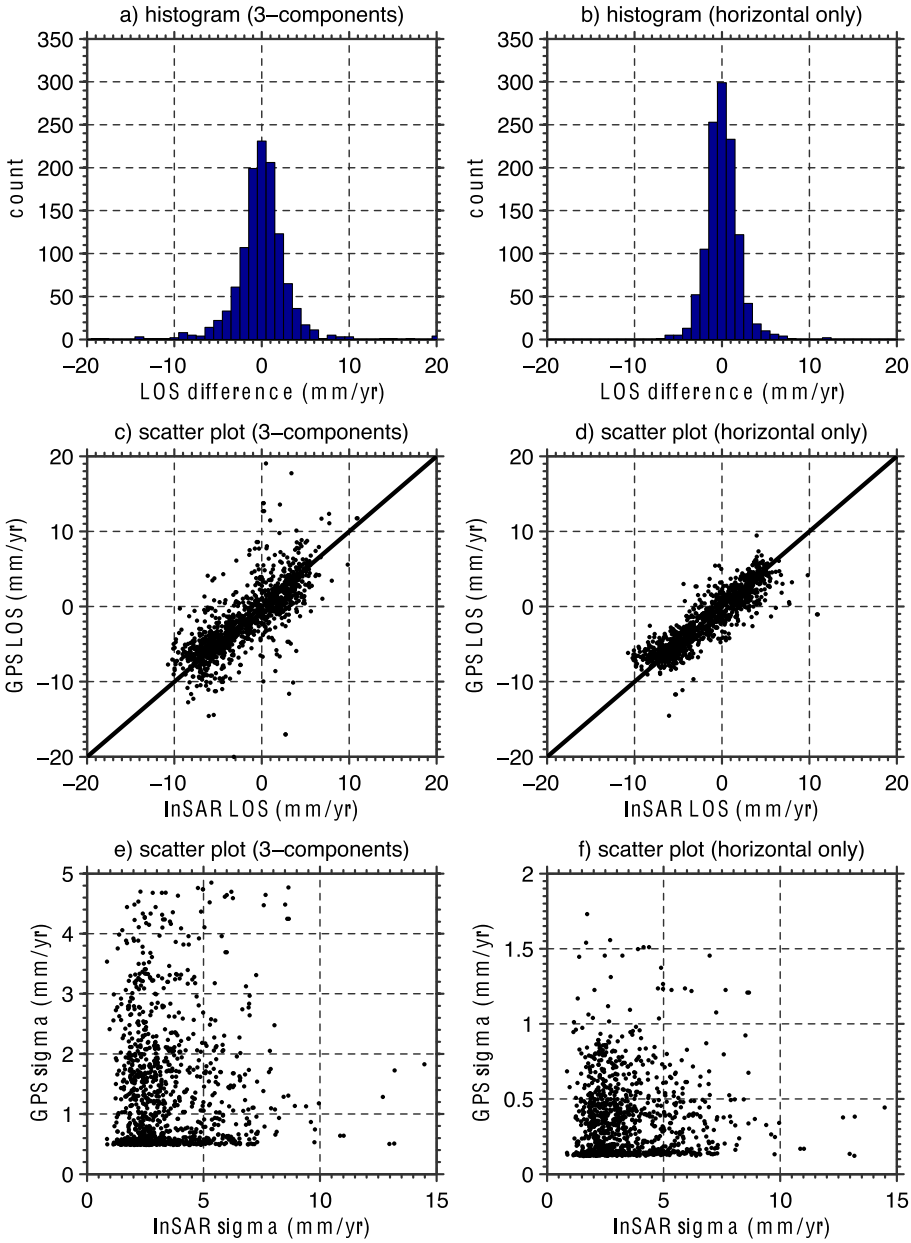

Figure 13. Comparison between the InSAR LOS velocity and the GPS observations projected into LOS coordinates. (a, b) Histogram of $V_{\text{diff}}(x) = V_{\text{GPS}}(x) - V_{\text{InSAR}}(x)$ for 1068 GPS sites. (c, d) $V_{\text{InSAR}}(x)$ against $V_{\text{GPS}}(x)$. (e, f) Comparison of the standard deviations $\sigma_{\text{GPS}}(x)$ and $\sigma_{\text{InSAR}}(x)$. Both the vertical and the horizontal components of the GPS velocity are used in the projection for Figures 13a, 13c, and 13e. Only the horizontal components of the GPS velocity are used in the projection for Figures 13b, 13d, and 13f.

creeping signal within 10 km from the fault trace. On the northern segment, the creeping section is creeping at ~4 mm/yr in LOS (~14 mm/yr in horizontal). The Paicines segment of the Calaveras fault is also creeping at 3–4 mm/yr in LOS. On the central segment of the creeping section, the ~7 mm/yr creep rate in LOS (~23 mm/yr in horizontal) is well recovered. On the southern segment of the creeping section, InSAR detects anomalous asymmetric ground motion within 3 km west of the fault zone. From Figure 12c, the rate of the motion is about –12 mm/yr near the fault trace and decreases to –6 mm/yr just 3 km west of the fault. The gradient associated with this LOS velocity change is 2 mm/yr/km, thus if we attribute this anomaly to horizontal simple shear in the vicinity of the fault zone and scale the LOS velocity into horizontal motion, the shear strain rate is 6 microstrain/yr. This large strain rate could be caused by the inelastic response of the fault zone material. Due to the ambiguity of the InSAR LOS direction, we could not detect if the ground is moving horizontally or vertically. Vertical motion could be caused by fluid flow within the porous brittle fault zone [*Byerlee*, 1993; *Wisely and Schmidt*, 2010]. As far as we know, this peculiar deformation signal on the creeping section and its cause has not been understood by previous workers. This apparent anomaly could also be caused by artifacts in the radar interferograms, such as a change in the surface reflective

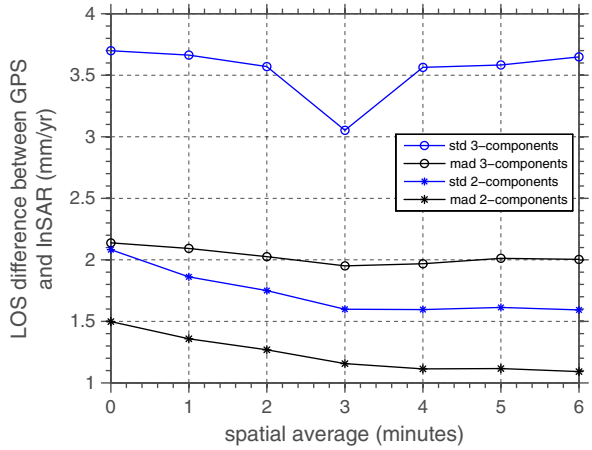

Figure 14. The standard deviations of $V_{diff}(x) = V_{GPS}(x) - V_{InSAR}(x)$ as a function of spatial averaging. "std" means the standard deviations and "mad" means the median absolute deviations. The horizontal axis is in arcminutes. One arcminute is approximately 2 km in distance. In the legend, 3-components represent both horizontal and vertical displacements while 2-components represent horizontal displacements only.

property. With additional ERS or Envisat satellite data or GPS data, it might be possible to resolve this issue.

4.2. Comparison With GPS LOS Data

[27] We compared the recovered LOS velocity $V_{InSAR}(x)$ with 1068 co-located GPS measurements (T. Herring, personal communication, 2011) to investigate the accuracy of $V_{InSAR}(x)$. We denote the projected GPS velocity vectors and their standard deviations as $V_{GPS}(x)$ and $\sigma_{GPS}(x)$. These are projected into the LOS direction using the precise orbital information from each satellite track. We divide our comparison results into two groups depending on whether the vertical velocity of the GPS vectors are included in the projection. The results are summarized in Figure 13. Figure 13a shows the histogram of the differences between the recovered LOS velocity and GPS measurements $V_{diff}(x) = V_{GPS}(x) - V_{InSAR}(x)$. The standard deviation and the mean absolute deviation of $V_{diff}(x)$ are 3.7 mm/yr and 2.1 mm/yr, respectively. Figure 13c shows the scatter plot between $V_{InSAR}(x)$ and $V_{GPS}(x)$. As expected, these two measurements are linearly correlated and the normalized correlation coefficient is 0.66 (1 means perfect correlation). Figure 13e shows that the uncertainties of the two measurements $\sigma_{GPS}(x)$ and $\sigma_{InSAR}(x)$ are not correlated as their correlation coefficient is only –0.05. The estimate of $\sigma_{InSAR}(x)$ includes seasonal effects that vary annually or semi-annually but the estimate of $\sigma_{GPS}(x)$ has these effects removed. When only the horizontal components of the GPS velocity are used in the projection (Figures 13b, 13d, and 13f), the standard deviation of $V_{diff}(x)$ reduces to 2.1 mm/yr, its mean absolute deviations is reduced to 1.5 mm/yr, and the correlation coefficient between GPS and InSAR measurements increases to 0.90.

[28] Since the InSAR data contains both signal and noise, we investigated how spatial averaging can improve the signal-to-noise ratio of the LOS velocity. A common way to improve the signal-to-noise ratio is to apply a moving-average window with a designated window size. We used the *GMT blockmedian* command to average LOS velocity $V_{InSAR}(x)$ at different spatial scales and then computed the standard deviations of $V_{diff}(x)$. Figure 14 shows how the standard deviations of $V_{diff}(x)$ vary as a function of spatial averaging. We present both the standard deviation and the mean absolute deviation of $V_{diff}(x)$. We consider the projected LOS velocity from GPS vectors both with and without vertical component. For the comparison using horizontal components of the GPS data, the mean absolute deviation of $V_{diff}(x)$ reduces from 1.5 mm/yr to 1.1 mm/yr after spatial averaging the InSAR data at 3 arcminutes (~6 km in distance) and remains constant for bigger average windows. For the comparison including vertical GPS velocity, the spatial averaging hardly changes the fit to the GPS data. As shown in Figure 14, including the vertical component of GPS velocity degraded the fit by ~25–50% compared to the case with only horizontal components, which could be caused by larger uncertainties in the vertical component of GPS data.

4.3. Power Spectrum

[29] The InSAR data add significant short wavelength noise and signal to the GPS-only model. We calculated the power spectrum (Figure 15a) of the GPS model and the LOS data, as well as their coherence spectrum (Figure 15b). Since estimating the power spectrum at a wavelength of 100 km requires a swath longer than 200 km, 12 long profiles, instead of 37 profiles, in Southern California were averaged

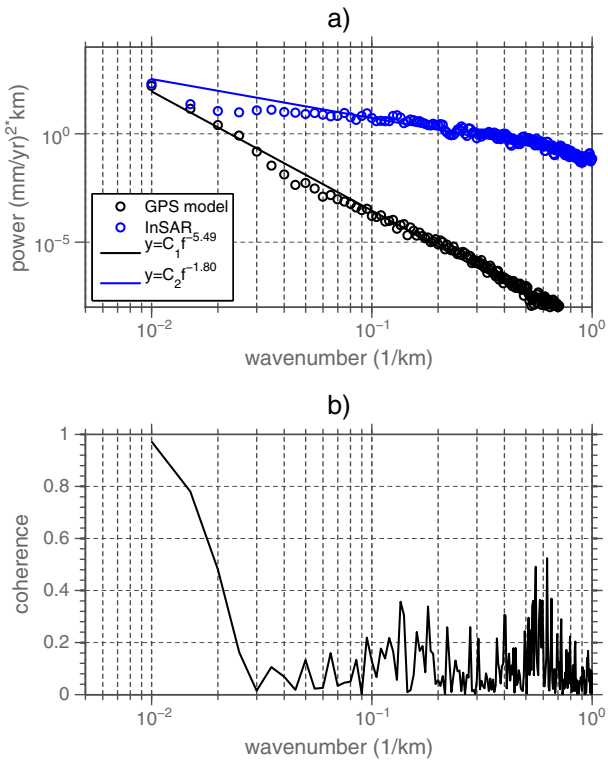

Figure 15. (a) Power spectrum of the GPS model and the InSAR LOS velocity data with their power law fitting curves. (b) Coherence spectrum between GPS model and the InSAR LOS velocity data.

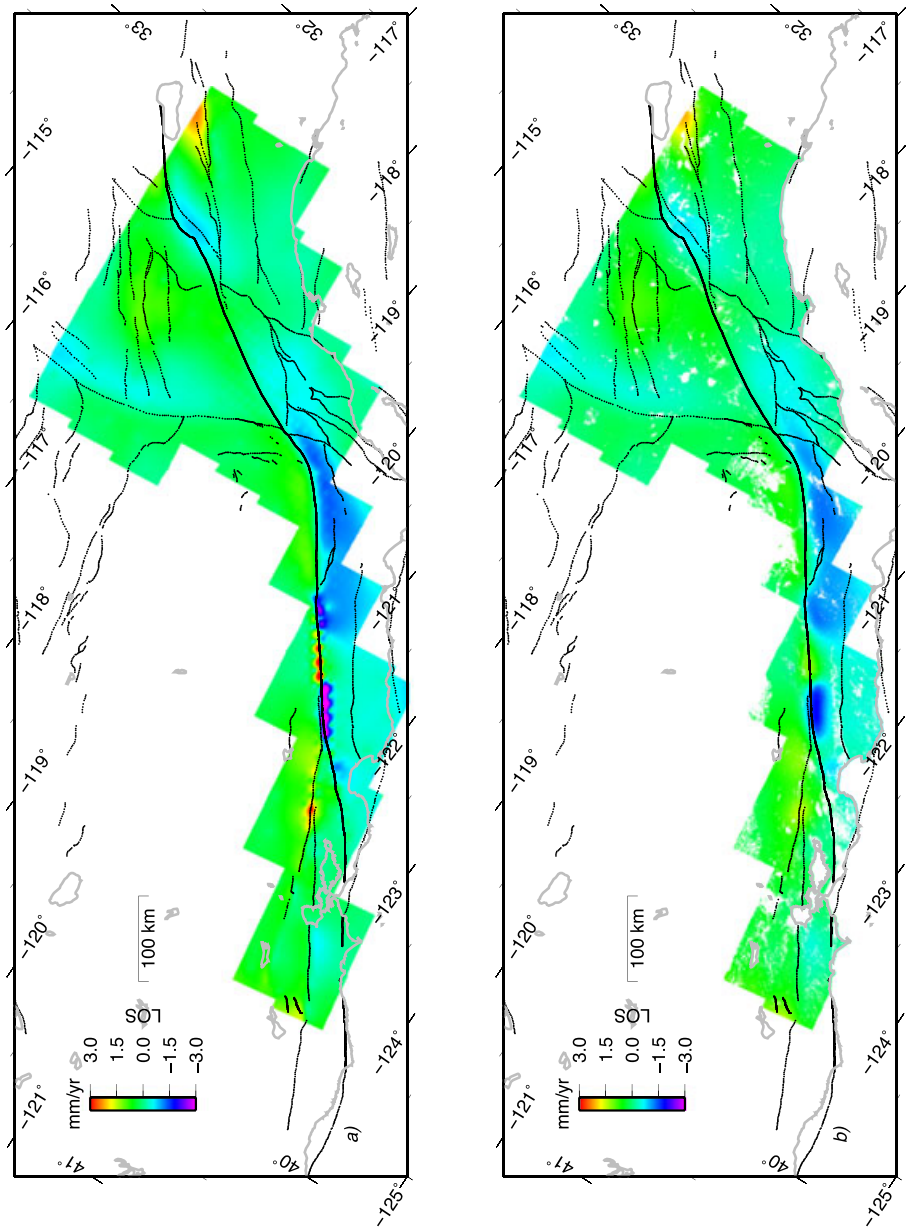

Figure 16. (a) The difference between the S-model and Z-model. The color represents the difference in LOS velocity. (b) The difference between the recovered high-resolution LOS velocity data using S-model and Z-model. The coverage of the LOS velocity map is smaller due to slightly smaller coverage of the Z-model.

to obtain a reasonable spectrum (marked in Figure 3a). At long wavelengths, the two spectra are at similar magnitude but their fall-off rates differ (Figure 15a). A power-law fitting to the power spectrum suggests that the spectrum of the GPS model falls off as $f^{-5.5}$, while the spectrum of the InSAR data falls off as $f^{-1.8}$ where f is the wave number. Although the power in the InSAR data could also be due to noise (i.e., atmosphere and ionosphere noise), many small-scale features, such as localized subsidence and fault creep, significantly contribute to the power over the short wavelengths, which could explain the difference in the fall-off rate. Figure 15b shows the coherence spectrum of the GPS model and the InSAR LOS velocity. The coherence reaches 0.95 at 100 km wavelengths, then decreases to below 0.2 at 15–40 km wavelength. This characteristic of the coherence spectrum is expected because the recovered InSAR LOS data contain the short wavelength signal not captured by the GPS.

4.4. Influence of the GPS Model

[30] The approach of combining GPS and InSAR relies on a model to interpolate the GPS-derived vector velocity field to the full resolution of the InSAR LOS data. Our premise is that the long-wavelength components of the model (>40 km) are well constrained by the GPS so the choice of the model should not have a significant effect on the

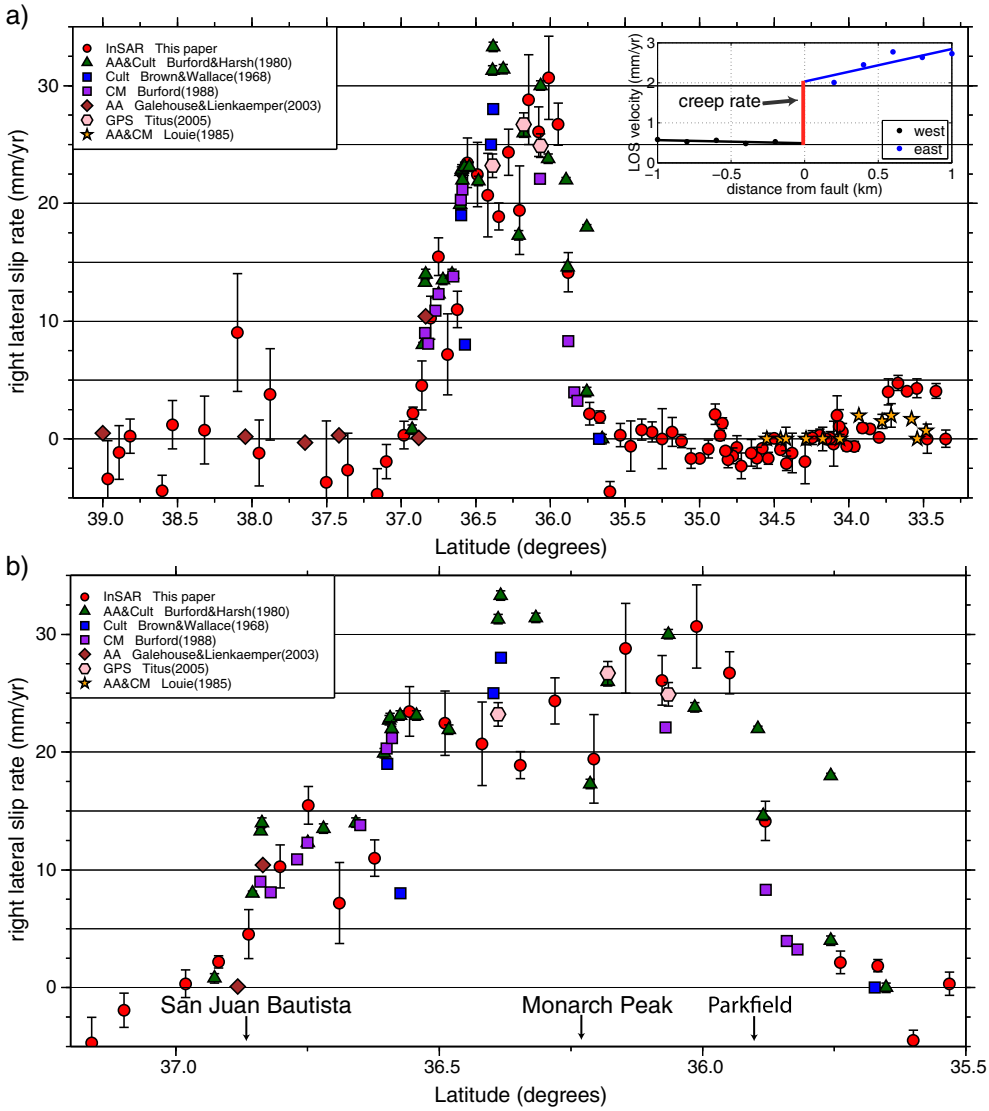

Figure 17. Creep rate comparison with an independent data set compiled by UCERF2. The red circles are the creep rate from InSAR in the period from 2006.5 to 2010 (this study). The error bars show the 1 σ (σ is the standard deviation) uncertainty. The triangles and other symbols are independent creep measurements compiled by UCERF2. AA means alignment array; CM means creep meters; Cult means cultural offset. (a) Creep rate along the entire SAF from north to south. The inset on the upper right corner shows the linear regression method to determine the surface creep rate across fault. (b) A zoomed-in view at the creeping section in central California. See text for details.

final LOS data. To investigate the effects of the model selection, we repeated the above GPS/InSAR integration analysis using the Z-model, instead of S-model. In both cases the vector velocities of the models were adjusted at long wavelengths to better match the GPS data so the residual misfits on the horizontal components are 1.8 mm/yr and 1.6 mm/yr for the S- and Z-models, respectively. The differences between the two models projected into the LOS are shown in Figure 16a. As expected there are large differences along the faults and in areas of high strain rate where the GPS spacing is insufficient to capture the full spatial resolution. In contrast, the differences between the two models after the integration of the InSAR data is smaller than 1 mm/yr, especially far from the faults (Figure 16b). There are two regions of larger difference: one along the creeping section and the other to the north of the Carrizo Plain. These are the areas where the S- and Z-models show larger initial disagreements perhaps due to differences in fault position or locking depth. However, away from these areas, the differences between the two models after integration are usually smaller than 1 mm/yr suggesting the analysis is not very sensitive to the choice of the long-wavelength starting velocity field.

5. Fault Creep

[31] We used the InSAR LOS data to estimate surface fault creep rate along the SAF system. Although many previous InSAR studies have measured fault creep rate over limited areas, this analysis is the first to provide

Table 2. Creep Rate on San Andreas Fault System

Latitude (degrees)	Longitude (degrees)	Creep Rate[1] (mm/yr)	Creep Rate Uncertainty (mm/yr)	Scale[2]
		San Andreas Fault		
33.349	–115.724	0.025	0.730	3.163
33.416	–115.799	4.074	0.629	2.643
33.475	–115.877	0.018	1.242	2.698
33.542	–115.951	4.299	0.802	3.075
33.608	–116.026	4.076	0.241	2.695
33.669	–116.102	4.762	0.642	2.902
33.734	–116.178	4.005	1.110	2.822
33.796	–116.255	0.139	0.138	2.666
33.856	–116.336	0.876	0.298	2.526
33.907	–116.422	0.939	0.396	2.360
33.962	–116.508	–0.618	0.410	2.475
34.013	–116.600	–0.598	0.393	1.938
34.042	–116.701	0.624	0.691	1.825
34.063	–116.806	1.089	1.413	1.772
34.078	–116.912	2.020	1.637	1.783
34.101	–117.017	–0.404	1.915	1.821
34.124	–117.121	0.081	0.537	1.845
34.151	–117.223	0.013	0.326	1.933
34.194	–117.319	0.346	0.505	2.175
34.245	–117.411	0.116	0.590	2.230
34.292	–117.503	–1.904	1.885	2.230
34.339	–117.597	–5.121	5.177	2.125
34.378	–117.694	–1.187	1.673	2.038
34.418	–117.791	–2.074	0.611	2.039
34.457	–117.888	–0.901	0.103	2.058
34.498	–117.985	0.056	0.241	2.059
34.539	–118.082	–1.640	0.509	2.059
34.578	–118.181	–0.798	0.304	2.001
34.616	–118.280	–1.602	0.884	1.983
34.652	–118.379	–1.176	1.137	1.984
34.688	–118.480	–5.093	0.956	1.920
34.719	–118.582	–2.272	1.089	1.888
34.749	–118.685	–0.701	0.982	1.888
34.777	–118.789	–1.425	0.675	1.862
34.808	–118.893	–1.755	0.681	1.919
34.824	–118.998	–1.012	0.345	1.730
34.846	–119.105	1.344	0.444	1.775
34.860	–119.211	0.298	0.413	1.868
34.895	–119.312	2.101	0.872	1.999
34.941	–119.405	–0.850	0.765	2.456
34.998	–119.492	–1.631	0.274	2.490
35.057	–119.575	–1.647	0.844	2.770
35.120	–119.655	–0.175	0.565	2.732
35.183	–119.732	0.602	1.220	3.020
35.250	–119.805	0.016	2.546	3.188
35.319	–119.877	0.609	0.857	3.199
35.387	–119.946	0.800	0.885	3.298
35.461	–120.013	–0.593	2.139	3.627
35.531	–120.081	0.338	0.987	3.361
35.600	–120.152	–4.464	0.845	3.052
35.667	–120.224	1.856	0.522	3.355
35.738	–120.294	2.143	0.963	3.357
35.823	–120.355	–5.286	3.173	3.086
35.880	–120.418	14.159	1.672	3.087
35.948	–120.493	26.732	1.783	3.056
36.011	–120.569	30.670	3.531	2.974
36.077	–120.645	26.096	2.101	2.853
36.146	–120.719	28.821	3.810	3.201
36.206	–120.790	19.429	3.770	2.902
36.280	–120.862	24.352	1.965	2.997
36.346	–120.935	18.891	1.152	3.119
36.419	–121.006	20.710	3.553	3.423
36.489	–121.077	22.461	2.733	3.167
36.556	–121.149	23.446	2.106	3.167
36.623	–121.223	11.006	1.550	2.955
36.689	–121.301	7.194	3.438	2.695
36.748	-121.384	15.479	1.590	2.402
36.802	–121.471	10.286	1.826	2.465
36.862	–121.557	4.543	2.084	2.722
36.919	–121.642	2.192	0.524	2.521
36.981	–121.724	0.343	1.174	2.871
37.098	–121.891	-1.910	1.456	2.315
37.160	–121.975	–4.693	2.182	2.799
37.357	–122.206	–2.632	3.124	3.481
37.500	–122.342	–3.671	5.213	3.898
37.877	–122.651	3.793	3.884	3.893
37.951	-122.715	–1.183	2.809	3.896
38.098	–122.846	9.042	5.003	3.696
38.319	–123.041	0.751	2.882	4.285
38.532	–123.250	1.216	2.051	3.292
38.603	–123.322	–4.390	1.316	3.425
38.673	–123.392	–8.293	3.702	3.428
38.743	–123.462	–8.131	2.212	3.431
38.817	–123.530	0.242	1.453	3.866
38.892	–123.596	–1.140	2.282	3.870
38.965	–123.661	–3.385	3.239	3.874
		Maacama fault		
38.786	–122.922	4.794	1.988	3.053
38.859	–122.993	–1.683	1.067	3.885
38.937	–123.048	8.481	5.452	5.635
39.018	–123.095	2.445	1.547	6.362
39.100	–123.143	2.749	1.301	6.372
39.181	–123.191	3.014	1.027	4.837
39.260	–123.248	–7.650	2.828	4.842
39.339	–123.305	0.846	2.700	4.848
39.420	–123.353	–6.367	6.170	6.319
39.502	–123.401	–8.432	6.456	6.085
39.584	–123.451	–13.417	3.456	6.091
39.665	–123.502	0.200	1.696	5.145
39.744	-123.557	-0.966	1.532	5.152
		Bartlett Springs fault		
39.038	–122.532	0.517	0.962	3.828
39.107	–122.623	1.776	1.369	3.270
39.170	–122.692	–4.980	2.055	2.443
39.234	–122.768	0.268	0.930	3.150
39.304	–122.833	–0.428	1.171	4.821
39.378	–122.899	–2.381	1.950	4.206
39.454	–122.959	–0.123	2.040	4.030
39.533	–123.020	6.946	4.026	5.388
		Concord fault		
37.972	–122.036	1.738	1.550	5.099
		Rodgers Creek fault		
38.170	–122.449	3.851	3.335	3.386
38.242	–122.520	–2.919	1.955	3.453
38.313	–122.594	–3.240	1.706	4.138
38.387	–122.654	2.083	2.017	4.204
38.465	–122.712	3.222	1.252	5.663
		Calaveras fault		
36.628	–121.189	7.420	2.063	3.053
36.697	–121.266	–0.533	1.552	3.214
36.766	–121.339	0.427	1.598	3.217
36.842	–121.396	5.190	2.051	5.806
36.924	–121.436	8.880	11.067	7.177
37.005	–121.483	7.157	2.284	4.660
37.084	–121.538	25.304	2.426	4.960
37.161	–121.598	9.220	1.458	3.971
37.238	–121.656	–3.419	1.843	4.612
37.315	–121.712	–3.855	4.634	4.617
37.392	–121.768	4.576	1.833	4.675
37.473	–121.819	–4.378	5.807	7.642

Table 2. (continued)

Latitude (degrees)	Longitude (degrees)	Creep Rate[1] (mm/yr)	Creep Rate Uncertainty (mm/yr)	Scale[2]
37.557	–121.859	14.671	6.272	11.950
37.640	–121.902	–2.585	2.477	5.413
37.721	–121.945	4.922	1.950	6.041
		Hayward fault		
37.526	–121.949	5.708	1.137	3.943
37.601	–122.012	2.505	0.946	3.425
37.673	–122.083	2.907	0.528	3.439
37.746	–122.143	1.291	0.586	3.557
37.821	–122.210	3.554	0.297	4.144
37.896	–122.270	4.910	0.718	4.243
		Garlock fault		
34.826	–118.867	0.448	0.532	1.821
34.881	–118.771	0.954	0.543	1.846
34.924	–118.676	0.366	0.572	1.746
34.965	–118.578	–0.619	0.305	1.711
34.995	–118.479	1.717	0.609	1.780
35.044	–118.386	–0.349	0.477	1.917
35.098	–118.296	–1.688	0.419	1.839
35.145	–118.203	0.518	0.261	1.850
35.190	–118.112	–0.025	0.077	1.871
35.246	–118.025	0.073	0.593	1.902
35.309	–117.944	–2.065	2.262	2.047
35.368	–117.860	0.255	1.099	1.829
35.412	–117.766	0.042	0.255	1.774
35.449	–117.665	0.548	0.150	1.705
35.477	–117.561	0.467	0.252	1.683
35.504	–117.456	–0.320	0.055	1.669
35.526	–117.349	0.302	0.187	1.675
35.551	–117.242	1.583	0.219	1.675
35.575	–117.136	0.516	0.190	1.675
35.595	–117.029	–0.702	0.210	1.666
35.604	–116.920	–0.360	0.097	1.665
35.596	–116.810	–0.088	0.091	1.665
35.593	–116.700	–0.869	0.483	1.682
35.591	–116.590	0.068	0.092	1.669
		San Jacinto fault		
33.033	–116.004	–1.629	1.614	2.898
33.099	–116.056	8.579	0.896	3.938
33.164	–116.143	2.212	1.180	2.675
33.222	–116.217	0.186	0.398	2.442
33.282	–116.296	–2.118	0.745	2.975
33.346	–116.371	-0.184	0.806	2.751
33.407	–116.453	-0.659	0.260	2.648
33.473	–116.516	–1.115	0.675	5.928
33.538	–116.588	0.709	0.569	2.872
33.594	–116.679	0.317	1.258	2.434
33.647	–116.763	1.189	1.053	2.255
33.698	–116.855	0.806	1.565	2.279
33.753	–116.952	2.230	1.063	2.280
33.815	–116.966	–12.948	2.936	2.496
33.877	–117.055	0.362	3.404	2.671
33.938	–117.135	–5.653	1.462	2.733
34.001	–117.215	1.442	0.678	2.946
34.067	–117.287	0.610	0.690	3.272
34.135	–117.358	6.505	2.733	3.274
34.198	–117.424	–0.316	2.192	2.417
34.253	–117.518	–0.875	2.281	2.283
34.311	–117.602	–0.308	1.204	2.594
		Superstition Hills fault		
32.923	–115.692	1.066	2.930	2.731
32.984	–115.769	2.786	0.400	2.478

[1]Positive creep rate implies right-lateral slip; negative creep rate implies left-lateral slip. [2]Scale is a factor that used to convert LOS to horizontal velocity.

comprehensive creep rate estimates for all the major faults of the SAF system over the time interval of the ALOS data acquisition 2006.5 to 2010. In addition to estimating creep rate, we also provide uncertainties and show comparisons with ground-truth measurements (Figure 17) such as GPS, alignment arrays (AA), creepmeters (CM) and cultural offsets (Cult) compiled in UCERF2 (Uniform California Earthquake Rupture Forecast, Version 2) [*Wisely et al*., 2008]. We performed the above analysis for the SAF, Maacama, Bartlett Springs, Concord, Rodgers Creek, Calaveras, Hayward, Garlock, San Jacinto, and Superstition Hills faults. The creep rate estimates, their geographic coordinates, and their uncertainties are summarized in Table 2.

5.1. Estimating Fault Creep Rate

[32] Here we record the best-fit creep rate across the fault trace from InSAR LOS velocity profiles. We used the method described by *Burford and Harsh* [1980] to determine the best-fit rates. The creep rate is quantified as an offset of the intercepts of the two best-fit linear functions (Figure 17 inset) at the fault trace (0 km distance). We took profiles of the high-resolution velocity grid perpendicular to fault strike. The profiles were spaced at 0.002° intervals in longitude along fault strike. The sampling interval across the fault was 0.2 km for 1 km on either side of the fault. The centers of the profiles were carefully chosen to reflect small bending sections of the fault traces. Then we averaged the profiles every 10 km along the fault strike. For each averaged profile, there were five LOS velocity data points on either side of the fault. In this analysis, we assumed no vertical motion across fault. We scaled the LOS velocity into horizontal direction considering variation of the fault strike. The quadratic mean of the residuals after linear regression was taken to be the error in the creep rate. We avoided making estimation if there were more than two data points missing in the averaged profiles on either side of the fault.

[33] We then compared our estimates with the compilation of creep measurements from *Wisely et al*. [2008] from various instruments (GPS, AA, CM, Cult) along the SAF (Figure 17). It should be noted that the InSAR measurement of fault creep represents the velocity difference on a scale of 200–300 m across the fault. In contrast, creepmeters and alignment arrays measure the velocity difference over a shorter distance of typically tens of meters to ∼100 m. Therefore, one would expect differences with the InSAR estimates being bigger unless the creep is really confined to a very small distance from the fault. Also note that the time period of these measurements is usually different. The alignment array surveys used in this comparison were mostly carried out in the 1970s and 1980s and while the GPS surveys and the InSAR observations are more recent and span a shorter time period. Despite these limitations, we found that the match between these independent measurements is satisfactory.

5.2. Creep Rate Results

[34] The InSAR-detected surface creep rates on the SAF are shown in Figure 17, along with records of the creep rates by other ground-based instruments. We did not find any significant creep signal on the SAF north of the Coachella segment and south of Parkfield. The dense alignment arrays and other instruments along the creeping section in Central

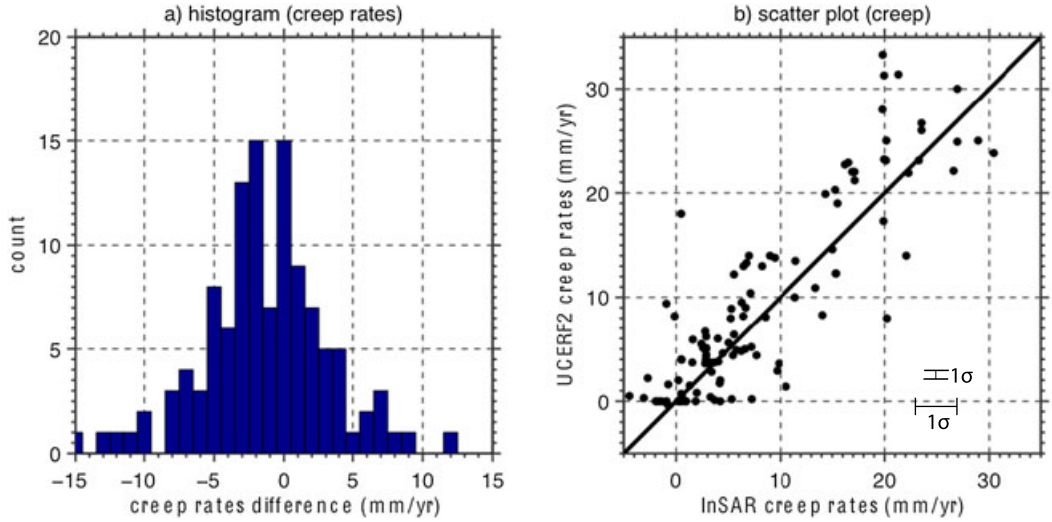

Figure 18. Creep rates estimates from InSAR and from ground-based instruments compiled by UCERF2 (alignment arrays, GPS, creepmeters, cultural offsets). (a) Histogram of the creep rates difference between InSAR and UCERF2 creep rate data sets. (b) Scatter plot of the creep rate data from InSAR versus UCERF2.

California provide a detailed kinematics of the fault creep [*Brown and Wallace*, 1968; *Burford and Harsh*, 1980; *Burford*, 1988; *Titus et al*., 2006]. As shown in Figure 17b, we found good agreement between the InSAR observations and the established measurements: creep starts at a "step-over" south of Parkfield and then increases northward. At Parkfield, the creep rate reaches 13 mm/yr. Between Monarch Peak and Parkfield, the creep rates are 25–30 mm/yr, which is compatible with the differential GPS survey by *Titus et al*. [2005] and alignment array surveys by *Burford and Harsh* [1980]. It is noteworthy that north of Monarch Peak (latitudes 36.2–36.4°), close to the Smith Ranch (Figure 5b), the creep estimates from InSAR are approximately 20–25 mm/yr, which is lower than the AA surveys of *Burford and Harsh* [1980] by 10 mm/yr. This discrepancy is somewhat unexpected and we discuss it in the following paragraphs.

[35] For creep rates obtained by alignment array method (AA), two different methods should be distinguished. In the study by *Burford and Harsh* [1980], two slip rates (best-fit rates and endpoint rates) are reported from repeated alignment array surveys on the SAF in Central California. The rates from the endpoint method are generally higher than the best-fit rates, sometimes by as large as 10 mm/yr [*Burford and Harsh*, 1980, Table 1]. *Burford and Harsh* [1980] used an example of simple shear distributed across the entire alignment array to justify that the best-fit rates underestimate the amplitude of actual creep. *Titus et al*. [2005] reported two different rates over the creeping section. They preferred the best-fit rate as a more robust method because it is less sensitive to noise in one single measurement. The best-fit rates reflect the amount of creep within the main slip zone and the endpoint rates probably include auxiliary fractures close to the main slip zone [*Burford and Harsh*, 1980, Figure 2].

[36] At the Smith Ranch site, the endpoint rates from *Burford and Harsh* [1980, Table 1] are 10 mm/yr larger than their best-fit rates. *Titus et al*. [2005, 2006] investigated this issue with GPS surveys and they found an average slip rate of 25 mm/yr at the fault, slower than the geological slip rate by about 10 mm/yr. The independent creep observation from InSAR in this study lends further support to the result from GPS survey [*Titus et al*., 2006]. The lower creep rate suggests that over the central segment of the creeping section the slip rate at the shallow portion of the crust is lower than the slip rate at depth (35 mm/yr) [*Ryder and Burgmann*, 2008; *Rolandone et al*., 2008].

[37] To the north of the creeping section, the InSAR-derived creep rates along SAF transition gradually to lower values as the other parallel faults, like the Calaveras Fault, the Rodgers Creek Fault and the Maacama Fault show signs of shallow fault creep. The creep estimates north of the San Francisco Bay area are contaminated by noise but in general they agree with previous results [*Galehouse and Lienkaemper*, 2003; *Funning et al*., 2007; *McFarland et al*., 2009]. *Funning et al*. [2007] found evidence for shallow fault creep at a rate up to 6 mm/yr along the Rodgers Creek Fault. Our study recovered a creep rate up to 3.8 mm/yr along the Rodgers Creek Fault (Table 2). *McFarland et al*. [2009] recovered creep rates of the faults of the San Francisco Bay region using theodolite measurements. They found the maximum creep rates along the Rodgers Creek Fault to be 4.2 mm/yr. *McFarland et al*. [2009] has found the creep rates along the Maacama Fault to be from 1.1 to 5.7 mm/yr. In this study, we found that the creep rates along the Maacama Fault varies from 0 to 8 mm/yr though the uncertainties are relatively large. As shown in Figure 17, certain estimates of creep rates are negative, which could suggest left-lateral creep or vertical movement across certain faults; however, most of these negative rates could reflect negligible surface creep when considering their uncertainties.

[38] *Louie et al*. [1985] surveyed three sites along the Garlock fault with alignment array methods. They found that the site near Cameron on the west Garlock Fault experienced a left-lateral creep of >4 mm/yr; two sites on the east Garlock Fault exhibited no creep. The InSAR-derived creep estimates supplement the alignment arrays that sparsely sampled the Garlock Fault. The LOS direction is more sensitive to the horizontal motion along the east-west trending fault compared to the northwest-southeast trending SAF. As

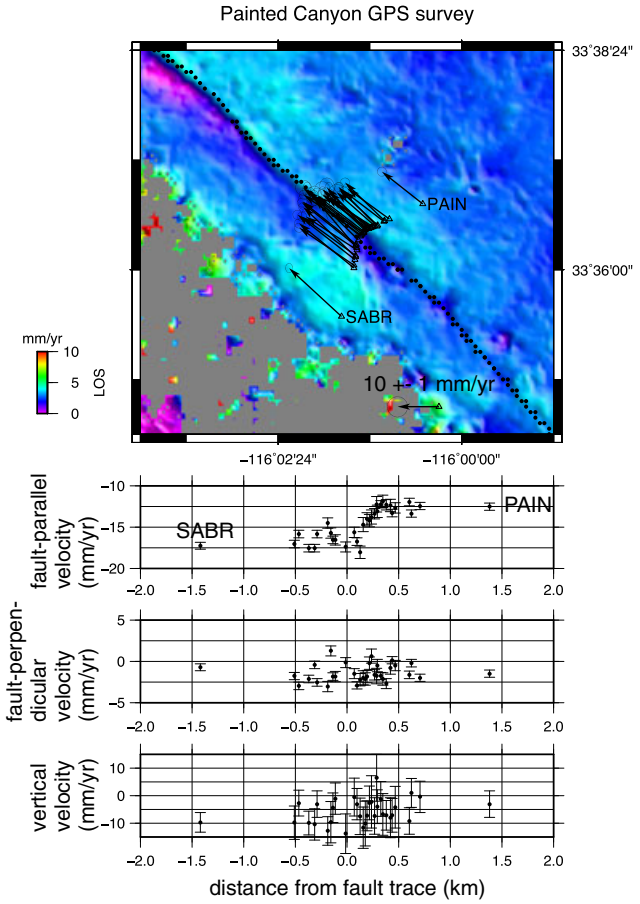

Figure 19. Campaign GPS survey at Painted Canyon in 2007 and 2010. The vectors in the top subplot show the horizontal GPS velocity, with 95% confidence ellipses. The black dots mark the SAF. The background is the recovered high-resolution LOS velocity map. Two base stations PAIN and SABR are labeled. The three bottom subplots show the fault parallel velocity, fault perpendicular velocity, and vertical velocity, respectively, across the fault trace.

shown in Table 2, we found no significant creep (<2 mm/yr) along the Garlock Fault from InSAR.

[39] The San Jacinto Fault is another fault that is not well instrumented with creep measurements. On the northern section of the San Jacinto Fault, we found no significant creep (<2 mm/yr), consistent with alignment array survey at the Clark Fault at Anza and the Claremont Fault at Colton by *Louie et al*. [1985]. *Louie et al*. [1985] documented aseismic slip on the Coyote Creek Fault at Baileys Well with a rate of 5.2 mm/yr since 1971. The InSAR data show an average creep rate of 8 mm/yr at the same location, in agreement with previous measurements [*Louie et al*., 1985].

[40] We computed the difference of the creep rates between InSAR and Uniform California Earthquake Rupture Forecast, Version 2 (UCERF2) at the corresponding locations along the SAF and other major faults. We utilized 115 creep data measurements for this comparison, ranging from 0 to 30 mm/yr. Taking the creep rate observations such as creepmeters and alignment arrays to be ground-truth, the overall accuracy of the InSAR-derived creep rates can be evaluated as the standard deviation of the creep rates difference, which is 4.6 mm/yr (Figure 18). The mean absolute deviation, which is less sensitive to outliers, is 3.5 mm/yr. A linear correlation with correlation coefficient of 0.86 is found between the InSAR data and the ground-truth observations.

5.3. Creep Rates From the Painted Canyon GPS Survey

[41] The surface creep rate at the Southern SAF Coachella segment near Painted Canyon is estimated to be 4–5 mm/yr from InSAR (Figure 17), whereas the rate from alignment arrays and creepmeters for the period of the 1970s to 1980s [*Louie et al*., 1985] is about 2 mm/yr. It is fortunate that 32 GPS monuments at Painted Canyon were surveyed in February 2007 and February 2010 by geophysicists from University of California, San Diego (UCSD). A. Sylvester from University of California, Santa Barbara (UCSB) installed most of the benchmarks in the 1980s for repeated leveling surveys. The 3 yr period of separation between the two surveys ensures that the differential displacement across the SAF exceeds the noise level [*Genrich and Bock*, 2006]. As shown in Figure 19, the creep rate is approximately 4.5 mm/yr and there is a 300 m wide deformed zone near the fault trace. No apparent fault-perpendicular velocity or vertical velocity can be distinguished. The excellent agreement between the InSAR and GPS observations validates our assumption that, at least in this area, there is negligible fault-perpendicular motion or vertical motion across the fault when projecting the radar LOS direction into horizontal motion.

[42] This difference between the creep rate from the 1970s to 1980s and the creep rate from 2007 to 2010 could be explained by the temporal variation of the surface creep. The geological creep rate [*Sieh and Williams*, 1990] in the past 300 yr is 2–4 mm/yr. The dense GPS array at Painted Canyon at almost the same time period of InSAR confirms an accelerated creep rate of 4–5 mm/yr. The nonsteadiness of creep on active creeping faults is not an unusual phenomenon and it can be, in general, attributed to a stress perturbation triggered by nearby earthquakes [*Lyons and Sandwell*, 2003; *Lienkaemper and Borchardt*, 1996]. We suspect that the creep rate from InSAR includes triggered creep from the 2010 El Mayor-Cucapah earthquake.

6. Conclusions

[43] Current interseismic velocity models based on GPS measurements alone cannot resolve features with short wavelengths (<15–40 km). L-band InSAR data are contaminated by errors at longer wavelengths from ionosphere, orbit (plane), and the atmosphere. To remedy these inadequacies, we recovered the interseismic deformation along the entire San Andreas Fault at a spatial resolution of 200 m by combining GPS and InSAR observations using a SURF approach. The integration uses a dislocation-based velocity model to interpolate the LOS velocity at the full resolution of the InSAR data in radar coordinates. The residual between the model and InSAR LOS velocity were stacked and high-pass filtered, then added back to the model. The filter wavelength is determined by a coherence spectrum analysis of four independent interseismic models. Future research should involve a spatially variable crossover

wavelength. The LOS velocity data are compared against 1068 GPS velocity measurements. These LOS velocity data and standard deviations are available to modeling groups for future use in their models. We have used these data to systematically estimate fault creep rate along the SAF and eight major faults and found a general agreement between InSAR and 115 published creep rate measurements. Our next step to advance this work will be to analyze, in detail, the LOS data away from the fault to estimate moment accumulation rate along major segments of the SAF.

[44] **Acknowledgments.** We thank Matt Wei, Sylvain Barbot, Leah Hogarth, Yariv Hamiel, Diane Rivet, Chris Takeuchi, Danny Brothers, Brent Wheelock, Rob Mellors, Duncan Agnew, Yuri Fialko, and Erica Mitchell for their participation in the 2007 and 2010 GPS surveys across the San Andreas Fault in Painted Canyon. We thank Yehuda Bock and Brendan Crowell for processing the GPS data from the Painted Canyon survey. The ALOS PALSAR L1.0 data were acquired through Alaska Satellite Facility (ASF). Tom Herring provided the GPS data used to constrain the interseismic velocity model. Duncan Agnew provided the fault traces. We thank Rob McCaffrey and Gareth Funning for reviewing the manuscript. This research was supported by the National Science Foundation (EAR 0811772, EAR 0838252, EAR0847499), NASA (NNX09AD12G), and the SCEC/UCERF-3 program.

References

Baxter, S. C., S. Kedar, J. W. Parker, F. H. Webb, S. E. Owen, A. Sibthorpe, and D. A. Dong (2011), Limitations of strain estimation techniques from discrete deformation observations, *Geophy. Res. Lett.*, *38*(L01305), doi:10.1029/2010GL046028.

Bird, P. (2009), Long-term fault slip rates, distributed deformation rates, and forecast of seismicity in the western united states from joint fitting of community geologic, geodetic, and stress direction data sets, *J. Geophys. Res.*, *114*(B11403), doi:10.1029/2009JB006317.

Brown, R. D. J., and R. E. Wallace (1968), Current and historic fault movement along the San Andreas fault between paicines and camp dix, California, in Conference on Geologic Problems of the San Andreas Fault System, vol. 11, edited by W. R. Dickinson and A. Grantz, pp. 22–39. Stanford University Publ. Geol. Sci., Menlo Park, California.

Burford, R. O. (1988), Retardations in fault creep rates before local moderate earthquakes along the san-andreas fault system, central california, *Pure Appl. Geophys.*, *126*(2–4), 499–529, doi:10.1007/BF00879008.

Burford, R. O., and P. W. Harsh (1980), Slip on the san-andreas-fault in central california from alignment array surveys, *Bull. Seismol. Soc. of Am.*, *70*(4), 1233–1261.

Byerlee, J. (1993), Model for episodic flow of high-pressure water in fault zones before earthquakes, *Geology*, *21*(4), 303–306, doi:10.1130/0091-7613.

Chen, C. W., and H. A. Zebker (2000), Network approaches to two-dimensional phase unwrapping: Intractability and two new algorithms, *J. Op. Soc. Am. A Op., Image Sci.*, *17*(3), 401–414, doi:10.1364/JOSAA.17.000401.

Demets, C., R. G. Gordon, D. F. Argus, and S. Stein (1990), Current plate motions, *Geophys. J. Int.*, *101*(2), 425–478, doi:10.1111/j.1365-246X.1990.tb06579.x.

Demets, C., R. G. Gordon, D. F. Argus, and S. Stein (1994), Effect of recent revisions to the geomagnetic reversal time-scale on estimates of current plate motions, *Geophys. Res. Lett.*, *21*(20), 2191–2194, doi:10.1029/94GL02118.

Emardson, T. R., M. Simons, and F. H. Webb (2003), Neutral atmospheric delay in interferometric synthetic aperture radar applications: Statistical description and mitigation, *J. Geophys. Res.*, *108*(B5), doi:10.1029/2002JB001781.

Eneva, M., and D. Adams (2010), Modeling of surface deformation from satellite radar interferometry in the salton sea geothermal field, california, *Trans. Geotherm. Resour. Counc.*, *34*, 527–534.

Farr, T. G., E. Rodriguez (2007), The shuttle radar topography mission, *Rev. Geophys.*, *45*(2), doi:10.1029/2005RG000183.

Fialko, Y. (2006), Interseismic strain accumulation and the earthquake potential on the southern San Andreas Fault system, *Nature*, *441*(7096), 968–971, doi:10.1038/nature04797.

Frank, F. C. (1966), Deduction of earth strains from survey data, *Bull. Seismol. Soc. Am.*, *56*, 35–42.

Freed, A. M., S. T. Ali, and R. Burgmann (2007), Evolution of stress in southern california for the past 200 years from coseismic, postseismic and interseismic stress changes, *Geophys. J. Int.*, *169*(3), 1164–1179, doi:10.1111/j.1365-246X.2007.03391.x.

Funning, G. J., R. Burgmann, A. Ferretti, F. Novali and A. Fumagalli (2007), Creep on the rodgers creek fault, northern San Francisco Bay area from a 10 year PS-InSAR dataset, *Geophys. Res. Lett.*, *34*(19), doi:10.1029/2007GL030836.

Galehouse, J. S., and J. J. Lienkaemper (2003), Inferences drawn from two decades of alinement array measurements of creep on faults in the san francisco bay region, *Bull. Seismol. Soc. Am.*, *93*(6), 2415–2433, doi:10.1785/0120020226.

Genrich, J. F., and Y. Bock (2006), Instantaneous geodetic positioning with 10-50 hz gps measurements: Noise characteristics and implications for monitoring networks, *J. Geophys. Res.*, *111*(B3), doi:10.1029/2005JB003617.

Goldstein, R. M., and C. L. Werner (1998), Radar interferogram filtering for geophysical applications, *Geophys. Res. Lett.*, *25*(21), 4035–4038, doi:10.1029/1998GL900033.

Gourmelen, N., F. Amelung, and R. Lanari (2010), Interferometric synthetic aperture radar-gps integration: Interseismic strain accumulation across the hunter mountain fault in the eastern california shear zone, *J. Geophys. Res.*, *115*(B09408), doi:10.1029/2009JB007064.

Hackl, M., R. Malservisi, and S. Wdowinski (2009), Strain rate patterns from dense gps networks, *Nat. Hazards*, *9*(4), 1177–1187.

Hearn, E. H., K. Johnson, and W. Thatcher (2010), Space geodetic data improve seismic hazard assessment in California: Workshop on incorporating geodetic surface deformation data into UCERF3; Pomona, California 12 April 2010, *Eos Trans. AGU*, *91*(38), 336, doi:10.1029/2010EO380007.

Johanson, I. A., and R. Burgmann (2005), Creep and quakes on the northern transition zone of the San Andreas Fault from gps and insar data, *Geophys. Res. Lett.*, *32*(14), doi:10.1029/2005GL023150.

Kreemer, C., W. E. Holt, and A. J. Haines (2003), An integrated global model of present-day plate motions and plate boundary deformation, *Geophys. J. Int.*, *154*(1), 8–34, doi:10.1046/j.1365-246X.2003.01917.x.

Lienkaemper, J. J., and G. Borchardt (1996), Holocene slip rate of the hayward fault at union city, california, *J. Geophys. Res.*, *101*(B3), 6099–6108, doi:10.1029/95JB01378.

Louie, J. N., C. R. Allen, D. C. Johnson, P. C. Haase, and S. N. Cohn (1985), Fault slip in southern-california, *Bull. Seismol. Soc. Am.*, *75*(3), 811–833.

Loveless, J. P., and B. J. Meade (2011), Stress modulation on the San Andreas Fault by interseismic fault system interactions, *Geology*, *39*(11), 1035–1038, doi:10.1130/G32215.1.

Lundgren, P., E. A. Hetland, Z. Liu, and E. J. Fielding (2009), Southern san andreas-san jacinto fault system slip rates estimated from earthquake cycle models constrained by gps and interferometric synthetic aperture radar observations, *J. Geophys. Res.*, *114*(B02403), doi:10.1029/2008JB005996.

Lyons, S., and D. Sandwell (2003), Fault creep along the southern san andreas from interferometric synthetic aperture radar, permanent scatterers, and stacking, *J. Geophys. Res.*, *108*(B1), doi:10.1029/2002JB001831.

McCaffrey, R. (2005), Block kinematics of the pacific-north america plate boundary in the southwestern united states from inversion of gps, seismological, and geologic data, *J. Geophys. Res.*, *110*(B07401), doi:10.1029/2004jb003307.

McFarland, F. S., J. J. Lienkaemper, and S. J. Caskey (2009), Data from theodolite measurements of creep rates on San Francisco Bay Region faults, California, 1979-2011 *Tech. rep., Open File Rep. 2009-1119*, U.S. Geological Survey.

Meade, B. J., and B. H. Hager (2005a), Block models of crustal motion in southern california constrained by gps measurements, *J. Geophys. Res.*, *110*(B3), doi:10.1029/2004JB003209.

Meade, B. J., and B. H. Hager (2005b), Spatial localization of moment deficits in southern california, *J. Geophys. Res.*, *110*(B4), B04,402, doi:10.1029/2004JB003331.

Molnar, P., and K. E. Dayem (2010), Major intracontinental strike-slip faults and contrasts in lithospheric strength, *Geosphere*, *6*(4), 444–467, doi:10.1130/GES00519.1.

Noriega, G. R., J. R. Arrowsmith, L. B. Grant, and J. J. Young (2006), Stream channel offset and late holocene slip rate of the san andreas fault at the van matre ranch site, carrizo plain, california, *Bull. Seismol. Soc. Am.*, *96*(1), 33–47, doi:10.1785/0120050094.

Parsons, T. (2006), Tectonic stressing in california modeled from gps observations, *J. Geophys. Res.*, *111*(B3), B03,407, doi:10.1029/2005JB003946.

Peltzer, G., F. Crampe, S. Hensley, and P. Rosen (2001), Transient strain accumulation and fault interaction in the eastern california shear zone, *Geology*, *29*(11), 975–978, doi:10.1130/0091-7613.

Pollitz, F. F., and M. Nyst (2005), A physical model for strain accumulation in the san francisco bay region, *Geophys. J. Int.*, *160*(1), 302–317, doi:10.1111/j.1365-246X.2005.02433.x.

Rolandone, F., R. Burgmann, D. C. Agnew, I. A. Johanson, D. C. Templeton, M. A. D'alessio, S. J. Titus, C. Demets, and B. Tikoff (2008), Aseismic slip and fault-normal strain along the central creeping section of the san andreas fault, *Geophys. Res. Lett.*, *35*(14), doi:10.1029/2008GL034437.

Rosen, P., C. Werner, E. Fielding, S. Hensley, S. Buckley, and P. Vincent Templeton (1998), Aseismic creep along the san andreas fault northwest of parkfield, ca measured by radar interferometry, *Geophys. Res. Lett.*, *25*(6), doi:10.1029/98GL50495.

Ryder, I., and R. Burgmann (2008), Spatial variations in slip deficit on the central san andreas fault from insar, *Geophys. J. Int.*, *175*(3), 837–852, doi:10.1111/j.1365-246X.2008.03938.x.

Sandwell, D., R. Mellors, X. Tong, M. Wei, and P. Wessel (2011), Open radar interferometry software for mapping surface deformation, *Eos Trans. AGU*, *92*(28), 234, doi:10.1029/2011EO280002.

Sandwell, D. T., and L. Sichoix (2000), Topographic phase recovery from stacked ers interferometry and a low-resolution digital elevation model, *J. Geophys. Res.*, *105*(B12), 28,211–28,222.

Savage, J. C., R. W. Simpson, and M. H. Murray (1998), Strain accumulation rates in the san francisco bay area, 1972–1989, *J. Geophys. Res.*, *103*(B8), 18,039–18,051, doi:10.1029/98JB01574.

Segall, P. (2002), Integrating geologic and geodetic estimates of slip rate on the san andreas fault system, *Int. Geol. Rev.*, *44*(1), 62–82, doi:10.2747/0020-6814.44.1.62.

Shen, Z. K., and D. D. Jackson (2005), Southern california tectonic deformation modeling, *Tech. rep.*, Southern California Earthquake Center.

Shen, Z. K., D. D. Jackson, and B. X. Ge (1996), Crustal deformation across and beyond the los angeles basin from geodetic measurements, *J. Geophys. Res.*, *101*(B12), 27,957–27,980, doi:10.1029/96JB02544.

Sieh, K. E., and P. L. Williams (1990), Behavior of the southernmost san-andreas fault during the past 300 years, *J. Geophys. Res.*, *95*(B5), 6629–6645, doi:10.1029/JB095iB05p06629.

Smith, B., and D. Sandwell (2003), Coulomb stress accumulation along the san andreas fault system, *J. Geophys. Res.*, *108*(B6), doi:10.1029/2002JB002136.

Smith, B., and D. Sandwell (2004), A three-dimensional semianalytic viscoelastic model for time-dependent analyses of the earthquake cycle, *J. Geophys. Res.*, *109*(B12), doi:10.1029/2004JB003185.

Smith, B. R., and D. T. Sandwell (2006), A model of the earthquake cycle along the san andreas fault system for the past 1000 years, *J. Geophys. Res.*, *111*(B1), B01,405, doi:10.1029/2005JB003703.

Smith-Konter, B., and D. Sandwell (2009), Stress evolution of the san andreas fault system: Recurrence interval versus locking depth, *Geophys. Res. Lett.*, *36*(L13304), doi:10.1029/2009GL037235.

Sneed, M., and J. T. Brandt (2007), Detection and measurement of land subsidence using global positioning system surveying and interferometric synthetic aperture radar, coachella valley, california, 1996–2005, *Scientific Investigations Report 2007*, 31 p., U.S. Geological Survey.

Titus, S. J., C. Demets, and B. Tikoff (2005), New slip rate estimates for the creeping segment of the san andreas fault, california, *Geology*, *33*(3), 205–208, doi:10.1130/G21107.1.

Titus, S. J., C. Demets, and B. Tikoff (2006), Thirty-five-year creep rates for the creeping segment of the san andreas fault and the effects of the 2004 parkfield earthquake: Constraints from alignment arrays, continuous global positioning system, and creepmeters, *Bull. Seismol. Soc. Am.*, *96*(4), S250–S268, doi:10.1785/0120050811.

Wei, M., D. Sandwell, and Y. Fialko (2009), A silent m(w) 4.7 slip event of october 2006 on the superstition hills fault, southern california, *J. Geophys. Res.*, *114*(B07), 402, doi:10.1029/2008JB006135.

Wei, M., D. Sandwell, and B. Smith-Konter (2010), Optimal combination of insar and gps for measuring interseismic crustal deformation, *Ad. Space Res.*, *46*(2), 236–249, doi:10.1016/j.asr.2010.03.013.

Welch, P. D. (1967), The use of fast fourier transform for the estimation of power spectra: A method based on time averaging over short, modified periodograms, *IEEE Trans. Audio Electroacoust.*, *AU-15*, 7073.

Williams, S., Y. Bock, and P. Fang (1998), Integrated satellite interferometry: Tropospheric noise, gps estimates and implications for interferometric synthetic aperture radar products, *J. Geophys. Res.*, *103*(B11), 27,051–27,067, doi:10.1029/98JB02794.

Wisely, B. A., and D. Schmidt (2010), Deciphering vertical deformation and poroelastic parameters in a tectonically active fault-bound aquifer using insar and well level data, san bernardino basin, california, *Geophys. J. Int.*, *181*(3), 1185–1200, doi:10.1111/j.1365-246X.2010.04568.x.

Wisely, B. A., D. Schmidt, and R. J. Weldon (2008), Compilation of surface creep on california faults and comparison of wgcep 2007 deformation model to pacific-north american plate motion, appendix p in the uniform california earthquake rupture forecast, version 2 (UCERF 2), *Open File Rep. 2007-1437P*, U.S. Geological Survey.

Zeng, Y., and Z.-K. Shen (2010), A kinematic fault network model of crustal deformation for california and its application to the seismic hazard analysis, *Tech. rep.*, U.S. Geological Survey.